PFC/JA-87-37

Numerical Modelling of Lower Hybrid RF Heating and Current Drive Experiments in the Alcator C Tokamak

Bonoli, P. T.; Porkolab, M.; Takase, Y. and Knowlton, S.

Plasma Fusion Center
Massachusetts Institute of Technology
Cambridge, MA 02139

October 1987

Submitted to: Nuclear Fusion

This work was supported by the U. S. Department of Energy Contract No. DE-AC02-78ET51013. Reproduction, translation, publication, use and disposal, in whole or in part by or for the United States government is permitted.

By acceptance of this article, the publisher and/or recipient acknowledges the U. S. Government's right to retain a non-exclusive, royalty-free license in and to any copyright covering this paper.

Numerical Modelling of Lower Hybrid RF Heating and Current Drive Experiments in the Alcator C Tokamak

Paul T. Bonoli, Miklos Porkolab, Yuichi Takase, Stephen F. Knowlton

Abstract

A simulation model is described for lower hybrid (LH) current drive, ramp up, heating, and sawtooth stabilization. The model incorporates a one-dimensional radial transport code, parallel velocity Fokker Planck calculation, and a toroidal ray tracing code. The Fokker Planck calculation includes the effects of the DC electric field, a perpendicular temperature due to pitch-angle scattering, and a loss term for fast electrons. The radial transport of fast electrons is described by a model diffusion equation. The toroidal ray tracing includes the effects of multiple radial reflections of the LH ray trajectories. For steady LH current drive it is found that the RF current generation is accurately predicted by a fast electron confinement time of the the form $\tau_L = \tau_o^{(\pm)}\gamma^3$, with $\tau_o^{(\pm)} = 3$ msec in the density range of $3 \times 10^{19}\mathrm{m}^{-3} \lesssim \bar{n}_e \lesssim 7 \times 10^{19}\mathrm{m}^{-3}$ [where $\pm$ distinguishes electrons moving parallel (antiparallel) to the current drive direction]. Also in this range, the theoretically predicted wave absorption and experimentally measured electron temperatures and stored energy were found to be consistent with an electron thermal diffusivity whose magnitude is independent of n_e. For LH ramp up, a significant increase in the negative RF current generation was found as $\bar{n}_e$ was lowered from $3\times10^{19}\,\mathrm{m}^{-3}$ to $1\times 10^{19}\,\mathrm{m}^{-3}$. This increase was due to the combined effects of the negative DC electric field and the presence of RF power in the anti-current drive direction. In order to reproduce the experimentally measured values of ramp up efficiencies, the negative RF current enhancement was minimized by reducing $\tau_o^{(-)}$ from 3 msec to 0.5 msec as

$\bar{n}_e$ was lowered from $3\times10^{19}\,\mathrm{m}^{-3}$ to $1\times10^{19}\,\mathrm{m}^{-3}$, with $\tau_o^{(+)} = (3-4)$ msec. For LH heating at densities $\bar{n}_e \simeq 1.4\times10^{20}\,\mathrm{m}^{-3}$, the experimental values of stored energy were found to be consistent with an electron thermal diffusivity whose magnitude is about 40% higher than that required in current driven discharges. Also for LH heating, the power lost due to collisional damping of the LH ray trajectories at the plasma periphery was found to be significant due to higher edge densities. Studies of LHRF sawtooth stabilization experiments with RF current drive indicated the possibility of creating stable profiles of the safety factor (q) via the generation of positive RF current near the $q = 1$ surface, thus producing a current "pedestal".

I. Introduction

In recent years lower hybrid waves have been successfully utilized for electron and ion plasma heating, to sustain and ramp toroidal plasma current, and to stabilize sawteeth in tokamaks.[1 – 8] In order to understand the underlying physics of these experiments, to make detailed comparisons between theory and experiment, and to extrapolate these results to the reactor regime, a considerable effort has been devoted to the development of simulation models for lower hybrid current drive (LHCD) and lower hybrid heating (LHH) [9 – 12]. Here we describe one such model[9 – 11] and its application to LHCD, LHH, and LH ramp up experiments in the Alcator C tokamak.[4, 7, 8, 13 – 16] This simulation model incorporates a $1-D$ radial transport code, a $1-D$ (parallel velocity) Fokker-Planck calculation, and a toroidal ray tracing calculation. An evolution equation is solved for the poloidal flux function $\psi(r,t)$ in conjunction with evolution equations for n_e, n_i, T_e, and T_i which are respectively the electron density, ion density, electron temperature, and ion temperature of the thermal plasma. The spatial loss of suprathermal electrons

generated by the LHRF is described by a model diffusion equation and the confinement of the electron tail is described by a phenomenological loss term in the Fokker Planck analysis. The Fokker Planck calculation also includes the effects of the parallel DC electric field and an arbitrary perpendicular (velocity) temperature due to pitch angle scattering. The toroidal ray tracing utilizes a Shafranov equilibrium and allows for multiple radial reflections of the rays near the plasma edge.[10]

In order to infer transport coefficients for thermal and suprathermal electrons, the wave absorption and driven RF current are calculated by combining a Fokker-Planck and a toroidal ray tracing analysis.[10] The confinement time of the electron tail is is fixed in this part of the calculation by the requirement that the driven RF current match that of the experiment for the same injected RF power (P_{in}). The wave absorption and RF current generation are then coupled to the transport analysis where the electron thermal diffusivity of the thermal plasma is adjusted so as to match the experimentally measured values of the central electron temperature and the stored energy.

One major finding of the numerical modelling is that the electron energy confinement properties of discharges maintained purely by lower hybrid driven current in Alcator C [4, 13 – 15] can be well-described by an electron thermal diffusivity whose magnitude is independent of electron density and an electron tail confinement time of the form [17] $\tau_L = \tau_o \gamma^3$, where $\tau_o \propto \tau_e, \gamma$ is the relativistic factor and τ_e is the electron energy confinement time of the thermal plasma. The discharges studied were in the range $3 \times 10^{19}\mathrm{m}^{-3} \leq \bar{\mathrm{n}}_\mathrm{e} \leq 1 \times 10^{20}\mathrm{m}^{-3}, 0.3\mathrm{MW} \leq \mathrm{P_{in}} \leq 1.0$ MW, and $I_p \simeq 140$ kA. Here $\bar{n}_e$ is the line average electron density, P_{in} is the injected LHRF power, and I_p is the toroidal plasma current. RF power lost due to finite electron tail confinement (P_L) was found to be significant at lower densities (in particular

at $\bar{n}_e = 3 \times 10^{19}\mathrm{m}^{-3}$, $P_L \simeq 0.3 \times P_{in}$) but was found to be less important at higher densities (in particular at $\bar{n}_e = 7 \times 10^{19}\mathrm{m}^{-3}$, $P_L \simeq 0.15 \times P_{in}$). A constant value of $\tau_o = 3$ msec was found to reproduce the correct RF current generation in this range of parameters (i. e. $I_{rf} \simeq 140$ kA, where I_{rf} is the radially integrated RF current).

An important result from the modelling of LH ramp up experiments in Alcator C was the enhancement in negative RF current generation which occurred as $\bar{n}_e$ was lowered from $3 \times 10^{19}\,\mathrm{m}^{-3}$ to $1 \times 10^{19}\,\mathrm{m}^{-3}$. This enhancement was due to the combined effects of a negative DC electric field and the presence of RF waves at $v_\parallel < 0$ in the injected power spectrum. Here $v_\parallel$ is the velocity parallel to the applied magnetic field and $v_\parallel > 0$ is taken to be the direction of the initial ohmic electric field drift of electrons. In order to reproduce the experimentally observed ramp up efficiencies, the increase in negative RF current at lower $\bar{n}_e$ was minimized by introducing separate confinement times $\tau_L^{(\pm)} = \tau_o^{(\pm)}\gamma^3$ for the tail electrons at $v_\parallel > 0$ (plus sign) and $v_\parallel < 0$ (minus sign). $\tau_o^{(-)}$ was then decreased from 3 msec to 0.5 msec as $\bar{n}_e$ was reduced from $3 \times 10^{19}\,\mathrm{m}^{-3}$ to $1 \times 10^{19}\,\mathrm{m}^{-3}$, with $\tau_o^{(+)}$ fixed at $(3-4)$ msec.

The simulation of high power ($P_{in} \gtrsim 1$MW) electron Landau heating experiments in Alcator C [7,8] at $\bar{n}_e \gtrsim 1 \times 10^{20}\mathrm{m}^{-3}$, and $B_\phi \gtrsim 5.5$ T indicated the importance of collisional damping of the LH waves in determining the overall power balance and heating. It was found that up to 30% of the injected RF power could be absorbed nonresonantly due to electron-ion Coulomb collisions at the plasma periphery. The confinement of suprathermal electrons was not an important issue at these higher electron densities since the slowing down time (τ_s) of fast electrons was much shorter than a typical tail confinement time (τ_o).

The simulation of RF sawtooth stabilization experiments in Alcator C [7] has

revealed the possibility of a novel stabilization mechanism. At $P_{in} \gtrsim 0.5$ MW, $\bar{n}_e \gtrsim 1.1 \times 10^{20}\mathrm{m}^{-3}$, and $B_\phi \simeq 6.2$ T, it has been found that the generation of RF current at $r \simeq r_1$ [where $q(r)$ is the safety factor and $q(r_1) = 1$] can result in a "flattening" of the $q(r)$ profile near r_1 so that $[dq(r)/dr]_{r_1} \approx 0$ and $q(0) \lesssim 1$. Recent predictions obtained using a fully toroidal and resistive MHD code indicate that such $q(r)$ profiles can be stable to the $m = 1$ mode.[18] The radially integrated RF current (I_{rf}) necessary to produce these profiles is found to be a small fraction of the total plasma current (I_p) with $I_{rf}/I_p \approx 0.1 - 0.2$. This is to be contrasted with the LHRF stabilization experiments carried out at lower density on the ASDEX tokamak where the stabilization mechanism was reported to be a raising of $q(r)$ above unity everywhere in the plasma.[6] However, at higher RF powers $0.6 \lesssim P_{in}(\mathrm{MW}) \lesssim 1$, code simulations of Alcator C indicate the more probable stabilization mechanism to be $q(r) > 1$ for $0 \leq r \leq a$.

The plan of this paper is as follows. The confinement models used for the thermal plasma transport are given in Sec. II. Section III is an outline of the evolution equation used for the poloidal flux function, describing the modifications to Ohm's Law due to the presence of a suprathermal RF current and the voltage boundary condition imposed at the plasma edge. Section IV is a review of the steady state Fokker analysis and contains a derivation of the spatial diffusion equation used for the suprathermal electron current. The wave propagation and absorption calculations are briefly reviewed in Sec. V and numerical results from the simulation model are presented in Sec. VI. Finally the conclusions are given in Sec. VII.

II. Thermal Plasma Transport Analysis

The $1-D$ radial transport code used in this model is essentially that described in Ref. [19]. The evolution equations for T_e and T_i are (in simplified form)

$$\frac{\partial}{\partial t} n_e T_e = \frac{1}{r}\frac{\partial}{\partial r} r n_e \chi_e \frac{\partial T_e}{\partial r} + S_d(r) - S_{ei}(r) + S_{oh}(r) - S_{rad}(r), \qquad (1a)$$

$$\frac{\partial}{\partial t} n_i T_i = \frac{1}{r}\frac{\partial}{\partial r} r n_i \chi_i \frac{\partial T_i}{\partial r} + S_{ei}(r), \qquad (1b)$$

where $\chi_e(\chi_i)$ are the electron (ion) thermal diffusivities, S_{ei} is the power density due to electron-ion collisional exchange, and S_{rad} is a radiative loss. $S_d(r)$ is an electron heating source due to the collisional slowing down of LHRF produced fast electrons during current drive and heating. $S_{oh}(r)$ is an ohmic heating source given by $J_{\|}E_{\|}$ where $J_{\|}$ is the total current density (parallel to the magnetic field) and $E_{\|}$ is the DC electric field given by the Ohm's Law relation discussed in Sec. III. Note that for steady-state LHCD $S_{oh}(r) \simeq 0$ since $E_{\|}(r) \simeq 0$. For simplicity the electron and ion densities are taken to be prescribed functions of time and position so that $\partial n_e(r,t)/\partial t = 0$ and $\partial n_i/(r,t)/\partial t = 0$. Although this assumption is certainly not necessary, it is an excellent approximation for LHCD and LHH.

The electron and ion thermal diffusivities are given by

$$\chi_i(r) = M_i \chi_i^{HH}(r), \qquad (2a)$$

$$\chi_e(r) = M_e \chi_e^{TANG}(r), \qquad (2b)$$

where χ_i^{HH} is the neoclassical form due to Hinton and Hazeltine.[20] The multiplier M_i is determined by matching to the observed central ion temperature of the ohmic plasma. Typically $M_i \simeq 3-6$ and M_i is assumed to be unchanged during RF injection. χ_e^{TANG} is derived from a microinstability-based model for anomalous electron thermal confinement [21] in conjunction with a "profile-consistent" form for $J_\parallel$[22, 23] and is given by,

$$\chi_e^{TANG}(r) = \frac{C_\mu^{0.4} 1.6 \times 10^4}{n_e(r)} \frac{a B_\phi^{0.3} Z_{eff}^{0.2}}{R_o^{1.9} q_a^{1.6}} \frac{a^2}{r^2} F(r), \tag{3a}$$

$$F(r) = \exp[\frac{2}{3}(q_a + 0.5)(r/a)^2] - \exp[-\frac{1}{3}(q_a + 0.5)(r/a)^2], \tag{3b}$$

with $n_e(10^{20}\mathrm{m}^{-3}), \mathrm{B}_\phi(\mathrm{T}), \mathrm{a(m)}, \mathrm{R_o(m)}, \chi_e(\mathrm{cm}^2/\mathrm{sec}), \mathrm{q_a = q(r = a)}, \mathrm{q(r)} = rB_\phi/[R_o B_o(r)]$ is the safety factor, and C_μ is a scaling constant. For ohmic discharges we take $M_e = 1$. $C_\mu \simeq 0.2$ was found to be an excellent fit to the ohmic electron temperatures observed in Alcator C at $1 \times 10^{19}\mathrm{m}^{-3} \lesssim \bar{\mathrm{n}}_\mathrm{e} \lesssim 1 \times 10^{20}\mathrm{m}^{-3}$ and $q_a \gtrsim 6$. At higher density ($\bar{n}_e > 1 \times 10^{20}\mathrm{m}^{-3}$) and $q_a < 6, C_\mu \simeq 0.5$ was found to yield excellent agreement between the ohmic simulation results and the experimental electron temperatures. During RF injection $M_e \geq 1$ was adjusted so as to obtain agreement with the experimentally observed central electron temperatures. It is thus possible to infer the magnitude of the electron thermal diffusivity which is consistent with both the experimentally observed electron temperatures and the theoretically predicted wave propagation and absorption.

III. Poloidal Field Evolution

The evolution equation for $\psi(r,t)$ is derived by starting with Maxwell's equations:

$$\frac{\partial}{\partial t}B_\theta(r,t) = \frac{\partial}{\partial r}E_\parallel(r,t), \tag{4a}$$

$$\frac{1}{r}\frac{\partial}{\partial r}rB_\theta(r,t) = \mu_o J_\parallel(r,t). \tag{4b}$$

Using $B_\theta(r,t) = \partial\psi(r,t)/\partial r$ in Eq. (4a) and integrating over r yields

$$\frac{\partial}{\partial t}\psi(r,t) = E_\parallel(r,t) + K(t). \tag{5}$$

The constant of integration $K(t)$ is determined by using a voltage boundary condition at $r = a$,

$$V_\parallel(a,t) = -L_{ext}\frac{d}{dt}I_p(a,t) + V_{OH}(t) + V_{EF}(t), \tag{6}$$

where $V_\parallel(a,t) = 2\pi R_o E_\parallel(a,t), L_{ext} = \mu_o R_o[ln(8R_o/a) - 2]$, $V_{OH}(t)$ is the voltage induced at the plasma edge due to changing current in the primary circuit of the ohmic heating (OH) transformer, and $V_{EF}(t)$ is the voltage induced at the plasma edge due to current changes in the coils of the vertical equilibrium field circuit. $K(t)$ can be evaluated using Eqs.(4b),(5) and (6)

$$K(t) = \frac{\partial}{\partial t}\psi(a,t) + \frac{a}{R_o}\frac{L_{ext}}{\mu_o}\frac{\partial}{\partial t}\left(\frac{\partial\psi}{\partial r}\right)_a - \frac{1}{2\pi R_o}[V_{OH}(t) + V_{EF}(t)]. \tag{7}$$

The appropriate Ohm's Law is constructed by recalling that

$$J_{\|}(r,t) = J_{OH}(t) + \tilde{J}_{rf}(r,t),$$

$$J_{OH}(r,t) = E_{\|}(r,t)/\eta_{\|}(r,t),$$

where $\tilde{J}_{rf}$ is the "diffused" suprathermal RF current calculated from a model diffusion equation described in Sec. IV. Combining the above expressions yields

$$E_{\|}(r,t) = \eta_{\|}(r,t)[J_{\|}(r,t) - \tilde{J}_{rf}(r,t)]. \tag{8}$$

The evolution equation for $\psi(r,t)$ is finally obtained by combining Eqs. (4b), (5), (7), and (8):

$$\frac{\partial}{\partial t}\psi(r,t) = \eta_{\|}\left[\frac{1}{\mu_o}\frac{1}{r}\frac{\partial}{\partial r}r\frac{\partial\psi}{\partial r}(r,t) - \tilde{J}_{rf}(r,t)\right] - \frac{1}{2\pi R_o}[V_{OH}(t) + V_{EF}(t)] + \frac{\partial}{\partial t}f(t), \tag{9a}$$

$$f(t) = \psi(a,t) + \frac{a}{R_o}\frac{L_{ext}}{\mu_o}\left(\frac{\partial}{\partial r}\psi\right)_a. \tag{9b}$$

Equation (9a) is solved in conjunction with Eqs. (1) subject to the radial boundary conditions $\partial\psi/\partial r = 0$ at $r = 0$ and $f(t) = 0$ at $r = a$.

V_{OH} is set to zero during steady state LHCD and ramp up since the primary circuit of the OH transformer is opened in these experiments. The contribution to $K(t)$ from $V_{EF}(t)$ should be small during steady state LHCD and LHH since I_p and β_θ do not vary in time after an initial transient phase. However, $V_{EF}(t)$ can play

an important role in reproducing the correct initial time behavior of $I_p(a,t)$ during LH ramp up. For Alcator C, $V_{EF}(t)$ will be given by [16]

$$V_{EF}(t) = -M_{\ell,EF}\frac{d}{dt}I_{EF}, \tag{10a}$$

$$I_{EF}(A) = 1 \times 10^4 B_V(T), \tag{10b}$$

$$B_V(T) = \frac{-\mu_o I_p}{4\pi R_o}\left[ln(8R_o/a) + \beta_\theta(a) + \frac{1}{2}l_i - \frac{3}{2}\right], \tag{10c}$$

$$l_i = \frac{2}{a^2}\frac{\int_o^a rB_\theta^2(r)dr}{B_\theta^2(a)}, \tag{10d}$$

where $\beta_\theta(a)$ is the total poloidal beta including the thermal plasma plus the electron tail, l_i is the internal inductance, and $M_{\ell,EF} = 150\mu H$ for Alcator C. Even if the kinetic (thermal electron and ion) part of $\beta_\theta(a)$ does not change during RF injection, there still can be a significant contribution to $V_{EF}(t)$ during the initial phase of LH ramp up due to a rapid increase in the electron tail pressure as the quasilinear plateau is populated in the electron distribution function.[24]

IV. Fokker-Planck Analysis

A. Steady-state Solution

The starting point for the Fokker-Planck analysis is an equation of the form

$$\frac{\partial}{\partial t}f_e = \frac{\partial}{\partial p_\parallel}D_{rf}(r,p_\parallel)\frac{\partial}{\partial p_\parallel}f_e + C(f_e) - eE_\parallel\frac{\partial f_e}{\partial p_\parallel} + \frac{1}{r}\frac{\partial}{\partial r}r\chi_{ef}\frac{\partial f_e}{\partial r} + \Gamma_s\delta(p_\parallel), \tag{11}$$

where $f_e = f_e(p_\perp, p_\parallel)$, $p_\perp(p_\parallel)$ is the component of momentum perpendicular (parallel) to the applied magnetic field, $p_\parallel = \gamma m_e v_\parallel, E_\parallel$ is the DC electric field, D_{rf} is the quasilinear RF diffusion coefficient [25], χ_{ef} is a diffusion coefficient for fast electrons, Γ_s is a source of particles at low $p_\parallel$, and $C(f_e)$ is the Landau limit of the Balescu-Lenard collision operator.[26, 27] Equation (11) is next reduced to a form which can be solved numerically at each radial grid point of the plasma and at each time step of the transport calculation. The procedure for doing this has been outlined in Ref. [10] and will be briefly reviewed here. It is assumed that the time scale on which f_e changes is fast compared to a transport time scale (τ_e) so that $\partial f_e/\partial t = 0$. The spatial diffusion term can be replaced by a phenomenological loss term of the form[17]

$$\tau_L^{(\pm)} = \tau_o^{(\pm)} \gamma^n, \tag{12}$$

where $\tau_o^{(\pm)} \propto \tau_e, n \geq 3$, and γ is the relativistic factor. Equation (12) is based roughly on the experimental measurements of runaway electron confinement times in PLT[17] and expresses the fact that suprathermal electrons will be better confined than thermal electrons. Equation (11) can be integrated over perpendicular momenta by assuming that f_e is a Maxwellian function in $p_\perp$ with an effective momentum spread of $(2m_e T_\perp)^{1/2}$,

$$f_e\left(p_\perp, p_\parallel\right) = \frac{F_e(p_\parallel)}{2\pi m_e T_\perp} \exp\left(-p_\perp^2/2m_e T_\perp\right), \tag{13a}$$

where m_e is the electron rest mass and $T_\perp$ is an effective temperature due to pitch-angle scattering. $F_e(p_\parallel)$ is a function of parallel momentum only and is normalized so that

$$\pi \int_o^\infty dp_\perp^2 \int_{-\infty}^\infty dp_\parallel f_e\left(p_\perp, p_\parallel\right) = 1. \tag{13b}$$

For $2T_\perp \ll m_e c^2, \gamma$ is approximated to be

$$\gamma^2 \simeq 1 + \frac{p_{\perp eff}^2}{\left(m_e c\right)^2} + \frac{p_\parallel^2}{\left(m_e c\right)^2},$$

where $p_{\perp eff}^2 \simeq 2 m_e T_\perp$. Applying $\pi \int_O^\infty dp_\perp^2$ to Eq. (11) and using Eqs. (12) and (13) yields

$$0 = \frac{\partial}{\partial p_\parallel} D_{rf}(r, p_\parallel) \frac{\partial F_e}{\partial p_\parallel} + \tilde{C}\left(F_e, T_\perp, p_\parallel, r\right) - eE_\parallel \frac{\partial F_e}{\partial p_\parallel} - F_e/\tau_L\left(p_\parallel\right) + \Gamma_s \delta\left(p_\parallel\right). \tag{14}$$

The collision operator $\tilde{C}$ is a rather complicated function given in Ref [10], and it may be expressed in terms of error functions. In the limit of $T_\perp = T_e$ and $\gamma \rightarrow 1, \tilde{C}(F_e)$ reduces to [24]

$$\tilde{C}\left(F_e\right) = \frac{2 + Z_i}{2} \nu_o \frac{\partial}{\partial p_\parallel} \frac{p_e^3}{p_\parallel^3} \left(p_\parallel F_e + \frac{1}{2} p_e^2 \frac{\partial}{\partial p_\parallel} F_e \right), \tag{15}$$

where Z_i is the ionic charge state, $p_e = m_e v_e, v_e = (2T_e/m_e)^{1/2}, \nu_o = \omega_{pe}^4 ln\Lambda/(2\pi n_e v_e^3)$, and $\omega_{pe} = (n_e e^2/\epsilon_o m_e)^{1/2}$.

A prescription for the perpendicular electron temperature was given in Ref. [10] and is based on the two-dimensional $(p_\perp, p_\parallel)$ Fokker-Planck solutions reported in Refs. [24,28,29]. The formulation used for $T_\perp$ can be summarized for $v_\parallel > 0$ by

$$T_\perp(\mathrm{keV}) = \mathrm{T_e}, \qquad 0 \leq \mathrm{v_\parallel} < \mathrm{v_1},$$

$$T_\perp(\mathrm{keV}) = \alpha_\perp \mathrm{T_e}, \qquad \mathrm{v_1} \leq \mathrm{v_\parallel} \leq \mathrm{v_2}.$$

Here v_1 and v_2 refer, respectively to the minimum and maximum values of parallel phase velocity for which $D_{rf} \gg \nu(v_\parallel)v_e^2/2$, where $\nu(v_\parallel) = \nu_o(v_e/v_\parallel)^3$. The maximum value of $\alpha_\perp$ for LHCD and LH ramp up is taken to be 50 and for LHH $\alpha_\perp = 20$. A similar formulation applies for $v_\parallel < 0$.

B. Moment Calculation

Once F_e is known at each radial grid point of the plasma, the RF current density J_{rf}, the RF power density S_{rf} that results from quasilinear electron Landau damping, the power density S_d that results from the collisional slowing down of fast tail electrons on thermal plasma electrons, the power density S_L that results from electron tail losses, and the energy density E_T stored in the electron tail can be calculated from

$$J_{rf}(r) = \int_{-\infty}^{\infty} dp_\parallel (n_e e v_\parallel) F_e(p_\parallel), \tag{16a}$$

$$S_{rf}(r) = \int_{-\infty}^{\infty} dp_\parallel n_e m_e c^2(\gamma - 1)\frac{\partial}{\partial p_\parallel} D_{rf}(p_\parallel)\frac{\partial}{\partial p_\parallel} F_e, \tag{16b}$$

$$S_d(r) = \int_{-\infty}^{\infty} dp_\parallel n_e m_e c^2(\gamma - 1)\tilde{C}(F_e), \tag{16c}$$

$$S_L(r) = \int_{-\infty}^{\infty} dp_\parallel n_e m_e c^2(\gamma - 1)\frac{F_e(p_\parallel)}{\tau_L(p_\parallel)}, \tag{16d}$$

$$E_T(r) = \int_{-\infty}^{\infty} dp_{\|} n_e m_e c^2 (\gamma - 1) F_e(p_{\|}). \tag{16e}$$

A useful moment to be calculated for comparison with experiment is the electron tail beta which is defined following Ref. [30] to be

$$\beta_\theta^{TAIL}(a) = \frac{2\mu_o}{B_\theta^2(a)} \left[\frac{1}{2} < P_{\phi\phi} > + \frac{1}{4} (< P_{rr} > + < P_{\theta\theta} >) \right], \tag{17a}$$

$$P_{\alpha\beta} = n_e m_e \int d^3p \gamma v_\alpha v_\beta f_e, \tag{17b}$$

where <> again denotes a volume average. The relativistic pressure tensor can be evaluated using Eq. (13) to yield

$$\beta_\theta^{TAIL}(a) = \frac{2\mu_o}{B_\theta^2(a)} \left\langle n_e T_e \int_{-\infty}^{\infty} dp_{\|} \gamma F_e(p_{\|}) \left[(v_{\|}/v_e)^2 + \frac{1}{2} T_\perp / T_e \right] \right\rangle \tag{18a}$$

We note that for $T_\perp = T_e$ and $\gamma \to 1$, $\beta_\theta^{TAIL}(a) = 2\mu_o < E_T(r) > / B_\theta^2(a)$. It is known from numerical solutions [24] of the time dependent, two-dimensional (velocity) Fokker-Planck equation that a finite time is required for the plateau in the electron distribution function to be populated. This turn-on time has been estimated to be [24]

$$\tau_{on} = 5(v_1/v_e)^2 [(v_2 - v_1)/v_e]^{1/2} \nu_o^{-1},$$

where the numerical coefficient is different than that given in Ref. [24] because of the different definition of v_e. Again v_1 and v_2 define the limits in parallel velocity

space for which D_{rf} is large. The time dependence of β_θ^{TAIL} can then be taken to be

$$\beta_\theta^{TAIL}(a,t) = \beta_\theta^{TAIL}(a)\{1 - \exp[-(t - t_{rf})/\tau_{on}]\}, \tag{18b}$$

where $\beta_\theta^{TAIL}(a)$ is given by Eq. (18a) and t_{rf} is the turn-on time of the RF power. For values of v_1, v_2, n_e and T_e typical of Alcator C, we have $\tau_{on} \simeq (3-5)$ msec.

C. Model Diffusion Equation for RF Current

In lower density ($\bar{n}_e \lesssim 3 \times 10^{19}\mathrm{m}^{-3}$) discharges in Alcator C, the slowing down time of fast electrons (τ_s) can be long enough so that $\tau_s \gtrsim \tau_e$. Then the earlier assumption of $\partial f_e/\partial t = 0$ on a transport time scale may not be an accurate approximation. A technique for treating the RF current density in this case was outlined in Refs. [9] and [11]. The procedure followed is to first apply an RF current density moment to Eqs. (11) and (14). The result is a diffusion equation of the form

$$\frac{\partial}{\partial t}\tilde{J}_{rf} = S_J(r) + \frac{1}{r}\frac{\partial}{\partial r} r \chi_{ef}(r) \frac{\partial}{\partial r}\tilde{J}_{rf} - \nu_J \tilde{J}_{rf}, \tag{19}$$

where S_J, χ_{ef}, and ν_J are calculated from the steady-state Fokker-Planck solution [Eq. (14)]. $\tilde{J}_{rf}$ is a "diffused" RF current density, to be distinguished from J_{rf} given by Eq. (16a). S_J represents a source of RF current density, χ_{ef} describes the spatial diffusion of RF current carriers, and ν_J gives the rate of momentum destruction for this current density.

The source S_J can be calculated by taking the RF current density moment of the quasilinear diffusion term in Eq. (14),

$$S_J(r) = \int_{p_1}^{p_2} n_e e v_\parallel dp_\parallel \frac{\partial}{\partial p_\parallel} D_{rf}(p_\parallel) \frac{\partial F_e}{\partial p_\parallel}, \tag{20}$$

where $p_1 = p_\parallel(v_1), p_2 = p_\parallel(v_2)$, and a similar expression applies for $p_\parallel < 0$.

The current density destruction rate ν_J is formulated by comparing the term $-\nu_J J_{rf}$ to the RF current density moment of the collision plus electric field terms in Eq. (14). The result is

$$\nu_J(r) = -\frac{C_\nu}{J_{rf}(r)} \int_{p_1}^{p_2} n_e e v_\parallel dp_\parallel \left[\tilde{C}(F_e) - eE_\parallel \frac{\partial}{\partial p_\parallel} F_e\right], \tag{21}$$

where C_ν is a scaling constant of order unity and $J_{rf}(r)$ is given by Eq. (16a). Again a similar expression applies for $p_\parallel < 0$.

An expression for $\chi_{ef}(r)$ can be deduced by first comparing a spatial diffusion term of the form $\frac{1}{r}\frac{\partial}{\partial r} r \chi_{ef} \frac{\partial J_{rf}}{\partial r}$ with the RF current density moment over the loss term in Eq. (14). The initial result is

$$\frac{\chi_{ef}}{\lambda_J^2} = \frac{C_\chi}{J_{rf}(r)} \int_{p_1}^{p_2} n_e e v_\parallel dp_\parallel \frac{F_e}{\tau_o \gamma^n},$$

where C_χ is a scaling constant of order unity and the spatial diffusion term has been approximated by taking $\partial/\partial r \sim \lambda_J^{-1}$ with $J_{rf}(r) \sim J_{rf}(0)\exp(-r^2/\lambda_J^2)$. The characteristic width of the RF current profile can be related to that of the electron temperature profile (λ_e) by assuming the profiles are approximately related by an Ohm's Law with a Spitzer resistivity so that $J_{rf} \sim J_\parallel \propto T_e^{3/2}$. Then $\lambda_e^2 = 3\lambda_J^2/2$, where $T_e = T_e(0)\exp(-r^2/\lambda_e^2)$ has been assumed. Using this result yields

$$\chi_{ef}(r) = \frac{2}{3} \frac{C_\chi \chi_e(r)}{J_{rf}(r)} \int_{p_1}^{p_2} n_e e v_\parallel dp_\parallel \frac{F_e}{\gamma^n}, \tag{22}$$

where we have taken $\tau_o \propto \tau_e$ and $\chi_e \sim \lambda_e^2/\tau_e$ for the thermal electron diffusivity. Again a similar analysis applies for $p_\parallel < 0$.

The numerical procedure for obtaining the "diffused" RF current density $\tilde{J}_{rf}$ is to solve the model diffusion equation [Eq. (19)] in conjunction with the transport equations [Eqs. (1)] and the evolution equation for ψ [Eqs. (9)]. Equation (19) is solved subject to the boundary conditions $(\partial \tilde{J}_{rf}/\partial r)_0 = 0$ and $\tilde{J}_{rf}(a) = 0$.[9] The terms S_J, χ_{ef}, and ν_J are obtained by evaluating Eqs. (20), (21), and (22) using the steady-state Fokker-Planck solution of Eq. (14). The constants C_ν and C_χ are adjusted so that the radially integrated RF current (I_{rf}) from Eqs. (14) and (16a) agrees with the radially integrated RF current ($\tilde{I}_{rf}$) from the diffusion equation [Eq. (19)]. From the preceding analysis, it can be seen that via the spatial diffusion of fast electrons it is possible to have a centrally peaked profile of RF current density ($\tilde{J}_{rf}$) although the source of fast electrons and RF current (S_J) is peaked off-axis. Rather than substituting $\tilde{J}_{rf}$ directly for J_{rf} in Ohm's Law, Eq. (8) is written in the form

$$E_\parallel(r,t) = \eta_\parallel(r,t)\left[J_\parallel(r,t) - J_{rf}(r,t) + J_{rf}(r,t-\Delta t) - \tilde{J}_{rf}(r,t-\Delta t)\right]. \qquad (23)$$

Equation (23) is then solved in conjunction with Eqs. (14) and (16a) since $J_{rf} = J_{rf}[E_\parallel(r,t)]$ is an implicit function of $E_\parallel$.

We conclude this section with a final point regarding the power density $S_d(r)$ due to the collisional slowing down of fast electrons. Since tail electrons can diffuse spatially as they slow down, it is more accurate to use the function $\tilde{S}_d(r)$ in Eq. (1a), where

$$\tilde{S}_d(r) = \tilde{S}_d(0)\tilde{J}_{rf}(r)/\tilde{J}_{rf}(0) \tag{24}$$

Thus, $\tilde{S}_d(r)$ has the same spatial profile as does $\tilde{J}_{rf}(r)$. $\tilde{S}_d(0)$ is chosen so the radially integrated values of $\tilde{S}_d(r)$ and $S_d(r)$ [from Eq. (16b)] agree. Equation (24) is used only at lower densities where the spatial diffusion of fast electrons is expected to be important (i. e., LHCD and LH ramp up). At higher densities Eq. (16c) is still used for $S_d(r)$ (i. e., LHH and sawtooth stabilization) where fast electrons would be expected to thermalize before they diffuse spatially.

V. Wave Propagation and Absorption

A. Ray Tracing

The wave propagation is treated in the geometrical optics limit using the ray equations,[31]

$$\frac{d\underline{x}}{dt} = -\frac{\partial D}{\partial \underline{k}} \Big/ \frac{\partial D}{\partial \omega}, \tag{25a}$$

$$\frac{d\underline{k}}{dt} = +\frac{\partial D}{\partial \underline{x}} \Big/ \frac{\partial D}{\partial \omega}, \tag{25b}$$

where $\omega, \underline{k}$, and D are taken to be real. Utilizing the Hamiltonian nature of these equations, [32] they take on a particularly simple form in toroidal geometry where $\underline{x} = (r, \theta, \phi)$ and $\underline{k} = (k_r, m, n)$ are the canonically conjugate momenta. Here r is the minor radial position, θ is the poloidal angle, ϕ is the toroidal angle, k_r is the radial wavenumber, $m = rk_\theta$ is the poloidal mode number, $n = (R_o + r\cos\theta)k_\phi$ is the toroidal mode number, and R_o is the torus major radius. $D(\underline{x}, \underline{k}, \omega)$ is the local

dispersion relation for LH waves including electromagnetic and thermal effects and is given by [10, 33]

$$D(\underline{x},\underline{k},\omega) = \alpha_t n_\perp^6 + \epsilon_\perp n_\perp^4 + \left[(\epsilon_\perp + \epsilon_\parallel)(n_\parallel^2 - \epsilon_\perp) + \epsilon_{xy}^2\right] n_\perp^2 + \epsilon_\parallel\left[(n_\parallel^2 - \epsilon_\perp)^2 - \epsilon_{xy}^2\right] = 0, \tag{26a}$$

$$\alpha_t = -\left[\frac{3}{2}\frac{\omega_{pi}^2}{\omega^2}\frac{v_i^2}{c^2} + \frac{3}{8}\frac{\omega_{pe}^2}{\omega_{ce}^2}\frac{\omega^2}{\omega_{ce}^2}\frac{v_e^2}{c^2}\right], \tag{26b}$$

$$\epsilon_\perp = 1 + (\omega_{pe}/\omega_{ce})^2 - (\omega_{pi}/\omega)^2\,, \tag{26c}$$

$$\epsilon_\parallel = 1 - (\omega_{pe}/\omega)^2 - (\omega_{pi}/\omega)\,, \tag{26d}$$

$$\epsilon_{xy} = \omega_{pe}^2/(\omega\omega_{ce})\,, \tag{26e}$$

where the cold plasma dielectric tensor elements of Stix [33] have been evaluated in the limit $\omega_{ce}^2 \gg \omega^2 \gg \omega_{ci}^2$. Here $n_\perp = k_\perp c/\omega, k_\perp$ is the component of $\underline{k}$ perpendicular to the applied magnetic field, $n_\parallel = k_\parallel c/\omega$, and $k_\parallel = \underline{k}\cdot\underline{B}/\mid\underline{B}\mid$. Also $v_i^2 = 2T_i/m_i, \omega_{pi} = (n_i e^2/\epsilon_o m_i)^{1/2}$ is the ion plasma frequency, and $\omega_{ce,i} = eB_o/m_{e,i}$ is the electron (ion) gyro-frequency. The effects of two-dimensional $(r-\theta)$ inhomogeneities of the tokamak equilibrium are accounted for in the wave propagation by taking $\underline{B} = \underline{B}(r,\theta)$ so that $D = D(r,\theta;k_r,m,n,\omega)$. $\underline{B}(r,\theta)$ is constructed from Shafranov's aspect ratio expansion.[10, 34] The parallel wavenumber will then vary due to the combined effects of magnetic shear and toroidicity (m variations) [10] since $dm/dt \propto \partial D/\partial\theta$ is nonzero from Eq. (25b). As shown in Ref. [10], these

toroidally induced variations in $k_\parallel$ can provide a possible mechanism by which LH waves injected at high parallel phase velocity [$v_\parallel \gtrsim 10 \times v_e$ and $n_\parallel \lesssim 1.5$] can have their phase velocities decreased. These slower velocity RF waves [$v_\parallel \gtrsim 3 \times v_e$ and $n_\parallel \lesssim 6$] can then undergo Landau interaction and generate a significant RF current.

Details of the model toroidal equilibrium used in the ray tracing have been given in Ref. [10]. Here we only mention that the zero-order cylindrical equilibrium quantities used in the aspect ratio expansion for $\underline{B}(r,\theta)$[34] are analytic functions which are fit to the profiles of $B_\theta(r), T_e(r), T_i(r)$, and $n_e(r)$ from the transport code. The analytic fits are

$$n_e^{(0)}(r) = (n_{eo} - n_{ea}) \frac{\exp(\epsilon_n) - \exp\left(\epsilon_n r^2/a^2\right)}{\exp(\epsilon_n) - 1} + n_{ea}, \tag{27a}$$

$$T_e^{(0)}(r) = (T_{eo} - T_{ea}) \frac{\exp\left(-\epsilon_e r^2/a^2\right) - \exp(-\epsilon_e)}{1 - \exp(-\epsilon_e)} + T_{ea}, \tag{27b}$$

$$T_i^{(0)}(r) = (T_{io} - T_{ia}) \frac{\exp(-\epsilon_i r^2/a^2) - \exp(-\epsilon_i)}{1 - \exp(-\epsilon_i)} + T_{ia}, \tag{27c}$$

$$B_\theta^{(0)}(r) = \frac{(\epsilon/q_o)\,(r/a)\,B_o}{1 + \epsilon_b\,(r/a)^2} \tag{27d}$$

Here n_{eo}, T_{eo}, and T_{io} are the central ($r = 0$) values of electron density, electron temperature, and ion temperature; n_{ea}, T_{ea}, and T_{ia} are the limiter ($r = a$) values of electron density, electron temperature, and ion temperature; $\epsilon = a/R_o$ is the inverse aspect ratio of the tokamak, and q_o is the central value of the safety factor. ϵ_b is determined from the total plasma current I_p and the relation

$B_\theta^{(0)}(a) = \mu_o I_p/(2\pi a)$. ϵ_e, ϵ_i, and ϵ_n are determined from the volume averages of $T_e(r), T_i(r)$, and $n_e(r)$ calculated in the transport analysis.

B. Wave damping

An evolution equation for the power flowing along the ray path is integrated simultaneously with the ray equations and has the form

$$\frac{dP}{dt} = -2\gamma_T P, \tag{28a}$$

$$\gamma_T = \gamma_e + \gamma_i + \gamma_c, \tag{28b}$$

where the focussing terms in (28a) have been neglected. The damping rate γ_e is a result of quasilinear electron Landau damping and γ_i is due to ion Landau damping (assuming unmagnetized ion orbits). γ_c is the nonresonant damping rate which results from electron-ion Coulomb collisions. γ_T is calculated in the weak damping limit ($\gamma_T \ll \omega$) to be [10]

$$\gamma_T = \left(\sum_{\alpha=e,i,c} D^{(\alpha)}(\underline{x}, \underline{k}, \omega) \right) \Big/ \frac{\partial D}{\partial \omega}, \tag{29a}$$

$$D^{(e)} = -\pi (m_e c)^2 \frac{\omega_{pe}^2}{\omega^2} \left(n_\perp^2 + n_\parallel^2 \right) \frac{\partial F_e}{\partial p_\parallel}, \tag{29b}$$

$$D^{(i)} = 2\pi^{1/2} \frac{\omega_{pi}^2}{\omega^2} n_\perp^4 \left(\frac{\omega}{k v_i} \right)^2 \exp\left(-\frac{\omega^2}{k^2 v_i^2} \right), \tag{29c}$$

$$D^{(c)} = \frac{\nu_{ei}}{\omega} \left(\frac{\omega_{pe}^2}{\Omega_{ce}^2} n_\perp^2 + \frac{\omega_{pe}^2}{\omega^2} n_\parallel^2 \right) n_\perp^2, \tag{29d}$$

where $\nu_{ei} = (2/3\pi^{1/2})\nu_o Z_{eff}$.

C. RF Diffusion Coefficient

An expression for the flux surface averaged, quasilinear diffusion coefficient due to the RF electric fields can be derived [10] by considering an increment of RF power $\Delta P(\underline{x}_{edge}, k_{\|}^o)$ launched near the plasma edge with initial parallel wavenumber between $k_{\|}^0$ and $k_{\|}^o + \Delta k_{\|}^o$ ($k_\perp = 0$). The RF power is assumed to propagate according to the ray equations and Eq. (28) in a "tube" of constant cross-section with varying group velocity. The result for the incremental diffusion coefficient acting on an electron contained within a volume $\Delta V(r)$ associated with two adjacent magnetic surfaces is [10, 25]

$$\Delta\bar{D}(r, v_{\|}, k_{\|}^o) = \frac{2\pi e^2}{\epsilon_o m_e^2} \frac{1}{\Delta V(r)} \sum_n Q_n, \tag{30}$$

$$Q_n = \int_{t_n}^{t_n+\Delta t_n} dt \delta(\omega - k_{\|}^n v_{\|}) \left(\frac{k_{\|}^2}{k^2}\right)_n \frac{\Delta P_n}{\frac{\partial}{\partial\omega}\left[\omega D / \left(n_\perp^2 + n_{\|}^2\right)^2\right]}.$$

Note that Eq. (30) has been expressed in MKS units rather than CGS units as done in Ref. [10]. The summation in Eq. (30) is over the number of transits the wave packet makes through the volume $\Delta V(r)$, t_n is the time the ray enters the volume and $t_n + \Delta t_n$ is the time the ray leaves the volume. Finally, $\Delta\bar{D}(r, v_{\|}, k_{\|}^o)$ must be summed over sufficiently many wavenumbers $k_{\|}^o$ representing the full range of the RF power spectrum [35] $P(k_{\|}^o)$, launched at the plasma edge. The result of this summation process is $D_{rf}(r, v_{\|})$.

It is clear from Eq. (30) that $D_{rf}(r, v_{\|})$ is an implicit function of the quasilinear electron Landau damping. Therefore the Fokker-Planck relation [Eq. (14)] must be solved in conjunction with Eq. (30) so that $D_{rf}(r, v_{\|})$ is consistent with the local wave damping. The procedure for doing this is to first evaluate D_{rf} assuming that $F_e \equiv F_e^{(0)}$ is Maxwellian. $D_{rf}^{(0)} = D_{rf}[F_e^{(0)}]$ is then used in Eq. (14) to generate the first approximation to the quasilinear $F_e \equiv F_e^{(1)}$. $F_e^{(1)}$ is used in Eq. (30) to calculate $D_{rf}^{(1)} = D_{rf}[F_e^{(1)}]$. $D_{rf}^{(1)}$ is then used in Eq. (30) to generate the second approximation to the quasilinear $F_e \equiv F_e^{(2)}$. This process is repeated until the radially integrated RF current moment does not change during successive iterations. Fifteen iterations are typically required at the start of the RF pulse with the RF power being turned on gradually in increments of $\Delta P_{in} = 0.1 \times P_{in}$. Only three to five iterations are required at subsequent time steps of the transport calculation.

VI. Simulation Model Results:

A. Numerical Details of Model

The transport, poloidal field, current diffusion, and Fokker-Planck calculations are all performed on a uniform radial grid with spacing $\Delta r_g = 0.025 \times a$. Typical time step sizes used in the transport code were $(0.5 - 2.0)$ milliseconds (msec).

The steady state distribution function $F_e(r, v_{\|})$ is obtained by solving Eq. (14) using a standard shooting technique.[10] Equation (14) is solved in the region of RF waves using a parallel velocity grid with nonuniform spacing $\Delta v_{\|} = v_{\|} \Delta n_{\|} / n_{\|}$. The velocity grid used below the region of RF waves (defined by $0 \lesssim v_{\|} \lesssim c/16.37$) has uniform spacing $\Delta v_{\|} = 0.05(c/16.37)$, i. e., twenty grid intervals. In addition to the normalization condition on F_e given by Eq. (13b), the runaway problem is

handled by taking $F_e(r, v_\parallel) = 0$ at $v_\parallel = \pm\infty$ and restricting $dF_e/dv_\parallel \leq 0$ for $v_\parallel > 0$ and $dF_e/dv_\parallel \geq 0$ for $v_\parallel < 0$.

The ray equations [Eqs. (25)] are integrated numerically using a predictor-corrector algorithm [10]. Since the thermal corrections to the LH dispersion relation have little effect on the ray trajectories in the current drive and electron heating regimes, it is possible to calculate the ray paths once and store pertinent quantities along each ray path. Only the wave damping [Eqs. (28)] and D_{rf} must be recalculated at each time step of the transport code due to changes in T_e and $F_e(r, v_\parallel)$. If $n_e(r)$ or $B_\theta(a)$ change significantly, it would also be necessary to recalculate the ray paths. The power spectra used in the Alcator C heating and current drive experiments [36] are shown in Figs. 1(a) and 1(b). Each spectrum is divided into fifty intervals or bars of power in the range $1 \leq \mid n_\parallel \mid \leq 8.37$, with a grid spacing of $\Delta n_\parallel = 0.044$ for $1 \leq \mid n_\parallel \mid \leq 1.99$ and $\Delta n_\parallel = 0.22$ for $1.99 \leq n_\parallel \leq 8.37$. A single ray is launched for each $\Delta n_\parallel$ interval, weighted to the appropriate power according to the calculated power spectrum.

B. Steady State LHCD Results:

Detailed code simulations were carried out for discharges in Alcator C maintained purely by LHRF driven currents.[4, 14, 15] The parameters used were $a = 0.165$ m, $R_o = 0.64$ m, $B_\phi = 8$ T, $I_p = 140$ kA, $\bar{n}_e = (3-7) \times 10^{19}$ m^{-3}, $Z_{eff} = 1.5$, hydrogen gas, $T_{eo} = (1.3 - 1.8)$ keV, $T_{io} = (0.6 - 0.8)$ keV, $M_i = 6$, relative waveguide phase $\Delta\phi = 90°$ [Fig. (1(a)], $\tau_L^{(\pm)} = \tau_o^{(\pm)}\gamma^3$, $\tau_{on} = 5$ msec, $f_o = 4.6$ GHz, and $P_{in} = (0.3 - 1.0)$ MW. The electron density was a prescribed function $n_e(r,t) = (n_{eo} - n_{ea})(1 - r^2/a^2)^\alpha n + n_{ea}$, where $n_{ea} = 0.15 \times n_{eo}$ and α_n was chosen so that $n_{eo}/\bar{n}_e = 1.5$. The results of these studies are summarized in Tables I-III.

Before discussing these results we first define certain terms used in these tables. The confinement times τ_E^{OH} and τ_E^{TOT} are given by

$$\tau_E^{OH} = \frac{W_B}{P_{oh}}, \tag{31a}$$

$$\tau_E^{TOT} = \frac{W_B + W_T}{P_{in}}, \tag{31b}$$

where the ohmic heating power (P_{oh}), the thermal plasma energy content (W_B), and the electron tail energy (W_T) are given by,

$$P_{oh} = (2\pi)^2 R_o \int_0^a J_\parallel E_\parallel r dr, \tag{32a}$$

$$W_B = (2\pi)^2 R_o \int_0^a \frac{3}{2}(n_e T_e + n_i T_i) r dr, \tag{32b}$$

$$W_T = (2\pi)^2 R_o \int_0^a E_T r dr, \tag{32c}$$

and $E_T(r)$ is given by Eq. (16e). The thermal or kinetic plasma beta is given by

$$\beta_\theta^K(a) = \frac{2\mu_o}{B_\theta^2(a)} < (n_e T_e + n_i T_i) >, \tag{33}$$

where <> denotes a volume average. The current drive "figure of merit" is taken to be

$$\tilde{\eta}(A/W/m^2) = \frac{\bar{n}_e(10^{20}\mathrm{m}^{-3})\mathrm{I_p(MA)R_o(m)}}{\mathrm{P_{in}(MW)}}. \tag{34}$$

Also, P_L, P_d, and P_{coll} are the volume integrated values of electron tail loss [Eq. (16d)], of power transferred collisionally from the electron tail to the thermal plasma [Eq. (16c)], and of power lost at the plasma periphery due to collisional damping of LH waves [Eq. (29d)].

The results in Tables I-III were obtained by first setting P_{in} to the value used in the experiment for a given electron density and plasma current. Then $\tau_o^{(+)} = \tau_o^{(-)}$ was adjusted until $I_{rf} \approx I_p$. The multiplier M_e was then varied until the values of T_{eo} and W_B in the code simulation agreed with those in the experiment. Finally, $C_\nu^{(\pm)}$ and $C_\chi^{(\pm)}$ were adjusted to achieve $\tilde{I}_{rf} \simeq I_p$. [That is, the radially integrated value of diffused RF current density from Eq. (19) was set equal to the radially integrated value of RF current density from Eqs. (14) and (16a).] As mentioned in Sec. IV C, typical values of $C_\nu^{(\pm)}$ and $C_\chi^{(\pm)}$ are very close to unity.

Several remarkable features appear in the results of Tables I-III. First, a constant value of $\tau_o^{(+)} = \tau_o^{(-)} = 3$ msec was found to reproduce the experimentally observed values of $\tilde{\eta}$ in Alcator C, in the range $\bar{n}_e = (3-7) \times 10^{19}$ m^{-3}. Furthermore, the values of M_e in Table II scale as $\bar{n}_e$, indicating that χ_e^{rf} is independent of electron density. [Recall from Eqs. (2b) and (3a) that $\chi_e = M_e \chi_e^{TANG}$ and $\chi_e^{TANG} \propto n_e^{-1}$.] Table III reveals the importance of the wave propagation and absorption physics when calculating the electron power balance. Although the injected RF power in these cases varied from $P_{in} = (0.32 \rightarrow 0.95)$ MW, the actual power coupled to the thermal plasma was considerably less, $P_d = (0.19 - 0.6)$ MW. At $\bar{n}_e = 3 \times 10^{19}$ m^{-3}, the power lost due to collisional damping of the LH rays was small but the electron tail loss was significant with $P_L \simeq 0.3 \times P_{in}$. However, at $\bar{n}_e = 7 \times 10^{19}$ m^{-3}, both these losses were comparable with $P_{coll} \approx P_L \simeq 0.15 \times P_{in}$. The importance of the electron tail energy in the overall power balance is clear from

Table II where $W_T \sim W_B \sim 1$ kJ at $\bar{n}_e = 3 \times 10^{19}$ cm^{-3} and as a consequence, $\tau_E^{TOT} > \tau_E^{OH}$. If τ_E^{TOT} were calculated ignoring the energy carried in the electron tail, the confinement time of the RF maintained discharges would be almost constant at $(3.5 - 3.7)$ msec. It can also be seen from Table II that the electron tail pressure as measured by $\beta_\theta^{TAIL}(a)$, contributes significantly to the total increase in $\beta_\theta(a)$ with $\beta_\theta^K(a) \sim \beta_\theta^{TAIL}(a) \sim 0.2$ at $\bar{n}_e = 3 \times 10^{19}$ m^{-3}.

The electron and ion temperatures of the bulk plasma were close to those of the RF maintained plasmas, as evidenced by the values of β_θ^K and W_B in Tables I and II. In fact, the central electron temperature decreased slightly during RF injection at $\bar{n}_e = 3 \times 10^{19}$ m^{-3} (from 1.6 to 1.5 keV). However at $\bar{n}_e = 7 \times 10^{19}$ m^{-3}, T_{eo} increased from 1.4 keV to 1.6 keV. The half-width of the electron temperature profile (λ_e) increased slightly during RF injection with $\lambda_e = (6.1 \rightarrow 6.5)$ cm at $\bar{n}_e \leq 5.5 \times 10^{19}$ m^{-3} and $\lambda_e = (6.1 \rightarrow 6.9)$ cm at $\bar{n}_e = 7 \times 10^{19}$ m^{-3}.

We next examine in detail, the results of the simulation model for the low density case ($\bar{n}_e = 3 \times 10^{19}$ m^{-3}) of Tables I-III. Figure 2(a) is the radial profile of dissipated RF power density due to electron Landau damping (S_{rf}) and Fig. 2(b) is the radial profile of diffused RF current density. Both plots correspond to a time of 100 msec after the RF has been turned on (t_{rf}). The radially integrated RF current corresponding to Fig. 2(b) is $\tilde{I}_{rf} = 134$ kA with 173 kA of positive RF current and 39 kA of negative RF current. The effect of diffusing the RF current density using Eq. (19) is clearly exhibited in Fig. 2(b). Although S_{rf} [and therefore J_{rf} from Eqs. (14) and (16a)] are peaked off-axis at $r \simeq 2.7$ cm, the profile of $\tilde{J}_{rf}$ is peaked on-axis and is rather flat for $0 \lesssim r \lesssim 3$ cm. This situation does not persist at higher density as shown in Figs. 3(a) and 3(b), where $S_{rf}(r)$ and $\tilde{J}_{rf}(r)$ are plotted for $\bar{n}_e = 7 \times 10^{19}$ m^{-3}. Clearly the effect of spatial diffusion of the RF current

density has been reduced since the profile of $\tilde{J}_{rf}$ is approaching that of $S_{rf}(r)$ (i.e., becoming peaked off-axis). The physical reason for this is that at higher density the collisional slowing down time of fast electrons is shorter than their spatial diffusion time scale, $\tau_d \sim \lambda_J^2/\chi_{ef}$. Thus, fast electrons are thermalized before they can diffuse spatially.

The radial profiles of $T_e(r)$ and $E_\parallel(r)$ are shown in Figs. 4(a) and 4(b) for the ohmic plasma and for the RF plasma (again at a time which is 100 msec after t_{rf}). As mentioned above, the width λ_e increases from 6.1 cm to 6.5 cm during RF injection. From Fig. 4(b) it can be seen that $E_\parallel(r) \simeq 0$ for $0 \leq r \leq a$, consistent with the notion that $\tilde{I}_{rf} \simeq I_p$ and $J_{rf}(r) \simeq J_\parallel(r)$ for steady state LHCD. The value of $E_\parallel(a)$ for the ohmic plasma corresponds to a loop voltage of $V_L = 1.4V$.

The time dependencies of V_L, I_p, and I_{rf} are shown in Figs. 5(a) and 5(b). An ohmic discharge is evolved for 50 msec and then the RF is turned at $t_{rf} = 50$ msec. The voltage $V_{OH}(t)$ is programmed so that $V_{OH} = 0$ for $t \geq t_{rf}$. The slight increase in I_p [Fig. 5(b)] during the RF pulse is due to the contribution of the voltage $V_{EF}(t)$ in the boundary condition for $V_\parallel(a,t)$ given by Eq. (6). V_{EF} is small and positive which causes I_p to increase in order to satisfy $V_\parallel(a,t) \simeq 0$ in the plasma.

The electron distribution function at a location corresponding to the maximum in the RF power deposition of Fig. 2(a), is plotted in Fig. 6 versus the parallel kinetic energy $E = m_e c^2[n_\parallel/(n_\parallel^2 - 1)^{1/2} - 1]$, for waves at positive and negative phase velocities. The endpoints of the plateaus in Fig. 6 are in good agreement with the limits imposed by wave accessibility [37, 38] [$n_{\parallel acc} = 1.258$ and $E(n_{\parallel acc}) = 322$ keV] and the condition for strong quasilinear electron Landau damping [37] [$n_{\parallel eld} \lesssim 5.7$ and $E(n_{\parallel eld}) \gtrsim 8$ keV]. The radial location ($r \simeq 2.7$ cm) shown in Fig. 6 corresponds to a local electron temperature of 1.3 keV. In terms of $v_\parallel/v_e$, the plateau extends

from $v_1/v_e = 2.46$ to $v_2/v_e = 11.15$. At lower energies ($E < 20$ keV and $n_\| \gtrsim 4.5$), the negative velocity plateau is higher in value than its counterpart for positive $v_\|$. This is not surprising since the injected power spectrum [Fig. 1(a)] is not purely unidirectional with about 30% of the RF power at $-6 \lesssim n_\| \lesssim -4$.

Although the injected RF power at positive $v_\|$ is restricted mostly to $n_\| \lesssim 2.5$, it is clear from Fig. 6 that some power has been shifted to lower phase velocities, via toroidally induced increases in the parallel wavenumber ($k_\|$). The physics of these phase velocity shifts in power [10] can be understood by examining the behavior of a single ray trajectory, shown in Figs. 7(a)-7(e). The initial value of parallel refractive index for this ray is $n_\| \equiv n_\|^0 = 1.594$. The poloidal projection of the ray path is shown in Fig. 7(a) and the normalized position (ρ/a), poloidal mode number (m), parallel refractive index ($n_\|$), and normalized wave amplitude (P_N) are plotted versus toroidal angle (ϕ) in Figs. 7(b)-7(e). The position ρ is $r + \Delta(r)\cos\theta$ where $\Delta(r)$ is the Shafranov shift.[34] The amplitude P_N is based on the quasilinear electron Landau damping due to the final $F_e(r, v_\|)$, for $v_\| > 0$ (shown at a single radius in Fig. 6). There is significant tail damping of the incident ray at high phase velocity ($n_\| \lesssim 1.8$ and $E \gtrsim 100$ keV) for $0 \lesssim \phi(\text{rad.}) \lesssim 6$, thus maintaining the quasilinear plateau at high $v_\|$. However, $n_\|$ increases to $2.8 - 3.5$ after two radial reflections of the ray near the plasma edge. This causes the remaining RF power in the wave to be damped at relatively high $n_\|$, thus maintaining the plateau at low phase velocity. Maintenance of the quasilinear plateau is therefore a detailed balance between LH wave absorption at high $v_\|$ (which determines the efficiency of the current drive process) and wave absorption at low $v_\|$ (which determines the plateau level; i.e., the electron tail population).

C. LH Ramp Up Results:

The total toroidal plasma current (I_p) can be increased with LHRF injection by raising the RF power above the level required for steady state current maintenance. Furthermore, the efficiency of this current ramp up process can be calculated from the rate at which RF power is converted to poloidal field energy. First consider the time rate change in the poloidal magnetic field energy (W_m), where W_m is defined as

$$W_m = \frac{1}{2} L_T I_p^2, \tag{35a}$$

and $L_T = L_{ext} + L_{int}$ is the total plasma inductance. L_{int} is given by,

$$L_{int} = \frac{(2\pi)^2 R_o}{\mu_o} \frac{1}{I_p^2} \int_0^a r B_\theta^2(r) dr. \tag{35b}$$

Applying the time derivative to W_m and using Eqs. (4),(6), and (35b) yields after some lengthy, but straightforward algebra

$$\frac{d}{dt}(\frac{1}{2} L_T I_p^2) = V_{EF} I_p - (2\pi)^2 R_o \int_0^a J_\parallel E_\parallel r dr. \tag{36}$$

If the external inductive power input, contributed from the equilibrium field circuit is identified as $P_{EF} = V_{EF} I_p$, the conversion efficiency can be defined as [16, 39]

$$\eta_{el} = \frac{\dot{W}_m - P_{EF}}{P_{in}} = -\frac{P_{oh}}{P_{in}}, \tag{37}$$

where the integral on the RHS of Eq. (36) has been identified as the ohmic heating power. Since η_{el} will in general vary with time we prefer to work with its time

averaged value ($\tilde{\eta}_{el}$) where

$$\tilde{\eta}_{el} = \frac{1}{\Delta t_{rf}} \int_{t_{rf}}^{t_{rf}+\Delta t_{rf}} \eta_{el}(t)dt. \tag{37b}$$

In this section we present simulation results (Table IV) of LH ramp up experiments in Alcator C.[16] The parameters used were identical to those of the previous section except that $Z_{eff} = 1.5 - 3.0, \Delta t_{rf} = 150$ msec, $\bar{n}_e = (1-3) \times 10^{19}\mathrm{m}^{-3}$, and $P_{in} \lesssim 0.5$ MW. The results in Table IV were obtained by setting P_{in} to a level of two to three times the RF power required for steady state current maintenance. Then $\tau_o^{(+)}$ and $\tau_o^{(-)}$ were adjusted to achieve the experimentally measured $\tilde{\eta}_{el}$. The most outstanding feature of these results is that $\tau_o^{(-)}$ had to be decreased from 3 msec to 0.5 msec to achieve an increase in $\tilde{\eta}_{el}$ as $\bar{n}_e$ was lowered from $3 \times 10^{19}\,\mathrm{m}^{-3}$ to $1 \times 10^{19}\,\mathrm{m}^{-3}$. If $\tau_o^{(-)}$ were to remain at 3 msec as $\bar{n}_e$ was lowered, a significant negative RF current would be generated, thus reducing $\tilde{\eta}_{el}$. This enhanced negative RF current generation occurs for two reasons. First, the tendency of the negative DC electric field to enhance $F_e(r, v_\parallel)$ over its Maxwellian value (at $v_\parallel < 0$) is more pronounced at lower electron density (since the electric field necessary to generate runaway electrons is reduced). Second, a significant fraction ($\sim 30\%$) of the incident RF power is launched at $-6 \lesssim n_\parallel \lesssim -4$, so that a plateau at $v_\parallel < 0$, can be maintained at a relatively high value, especially at lower energy ($E \lesssim 20\,\mathrm{keV}$). One way to reduce this enhanced negative RF current in the simulation model is to degrade $\tau_o^{(-)}$. To demonstrate how the effect of the negative DC electric field becomes more pronounced as $\bar{n}_e$ is reduced, we have given the values of v_{ph}/v_r in Table IV. Here the runaway velocity is $v_r = [n_e e^3 ln\Lambda/(4\pi\epsilon_o^2 m_e E_o)]^{1/2}$, where $E_o = \mid E_\parallel(r=0) \mid$, and v_r is evaluated at the plasma center since this is where fast electrons are expected to be concentrated. A value of $v_{ph} = c/ < n_\parallel > \approx 0.2 \times c$ is

used since the average $n_\parallel$ of waves at $v_\parallel < 0$ is $< n_\parallel > \simeq 5$. As $\bar{n}_e$ is reduced from $3 \times 10^{19}\mathrm{m}^{-3}$ to $1 \times 10^{19}\,\mathrm{m}^{-3}$, v_{ph}/v_r increases from 0.25 to 0.65, indicating that RF waves at $v_\parallel < 0$ are interacting with electrons closer to the runaway velocity at lower electron density. It is important to remember however, that for the density range in Table IV and for the RF power spectrum launched in the experiment, one does not expect a reverse runaway tail of electrons to be produced since $v_{ph}/v_r < 1$.

To illustrate the points made above, we show results of the simulation model in Figs. 8-10 for the $\bar{n}_e = 1 \times 10^{19}\,\mathrm{m}^{-3}$ case in Table IV. The RF current density in Fig. 8(a) is somewhat hollow on-axis. However, the RF deposition profile (not shown) is peaked at $r \simeq 5$ cm, so that fast electrons have diffused inward an appreciable distance. The radially integrated current in Fig. 8(a) is $\tilde{I}_{rf} = 170$ kA with 222 kA of positive RF current and 52 kA of negative RF current. Figure 8(b) indicates the electric field on-axis is -0.1 V/m during the RF pulse. Note that the ohmic electric field in Fig. 8(b) is changing with radius because V_{OH} was set to zero at $t = t_{rf} - 30$ msec, (so that I_p would be decreasing before the RF was turned on). Both RF plots in Fig. 8 correspond to a time of 150 msec after the RF turn-on.

Figures 9(a)-9(c) show $V_L, I_p, \tilde{I}_{rf}$, and $\tilde{\eta}_{el}$ as a function of time. The initial ramp rate in Fig. 9(b) is large with $\dot{I}_p \sim 900$ kA/sec for $t_{rf} \leq t \leq t_{rf} + 10$ msec. This is due to a significant positive contribution to the boundary condition on $V_\parallel(a,t)$ [see Eq. (6)] from V_{EF} as the electron tail is populated and β_θ^{TAIL} increases. However, this effect subsides after the initial turn on time of the tail (τ_{on}) and when averaged over the entire pulse length, $\dot{I}_p \sim 314$ kA/sec. The conversion efficiency shown in Fig. 9(c) has a time averaged value of $\tilde{\eta}_{el} \simeq 0.14$. The sudden changes in the plots shown in Fig. 9 are a numerical artifact due to the ray paths being recalculated at regular intevals (each time I_p changes by 5 kA during the first 30 msec of the RF

pulse).

Finally, we plot the distribution function for this case in Fig. 10, corresponding to a radial location of 4.95 cm (the maximum in the RF power deposition). It is interesting to compare the distribution functions for $v_{\|} < 0$ in Figs. 6 and 10. The effect of the negative DC electric field is clear in Fig. 10, where the plateau at $E \lesssim 20$ keV is about a factor of five higher than in Fig. 6. This feature persists even out to higher energies, $E \lesssim 100$ keV.

D. Lower Hybrid Heating Results:

The simulation model has also been used to analyze the results of high power electron Landau heating experiments in Alcator C.[7, 8] The parameters used were $a = 0.165, R_o = 0.64\text{m}, \text{B}_\phi = 5.5\text{T}, \text{I}_\text{p} = 256\text{kA}, \bar{\text{n}}_\text{e} = 1.4 \times 10^{20}\text{m}^{-3}, \text{Z}_\text{eff} = 1.5$, deuterium gas, $M_i = 2$, relative waveguide phase of 180° [Fig. 1(b)], $\tau_L^{(\pm)} = \tau_o^{(\pm)}\gamma^3, \tau_o^{(\pm)} = 14$ msec, $f_o = 4.6\,\text{GHz}$, $\Delta\text{t}_\text{rf} = 130$ msec, and $P_{in} = 1.0$ MW. The electron density was taken to be $n_e(r,t) = (n_{eo} - n_{ea})(1 - r^2/a^2)^\alpha n + n_{ea}$, where $n_{ea} = 0.15 \times n_{eo} = 1.27$. The voltage $V_{OH}(t)$ was programmed so that $\dot{I}_p = 0$ during the ohmic and RF pulses.

The power balance results for this case can be summarized as follows. A value of $M_e = 2.3$ was chosen so that the code results for T_{eo}, T_{io}, and W_B matched those of the experiment for the same injected RF power. The central T_e rise was $\Delta T_{eo} = 0.56$ keV from an initial value of $T_{eo} = 1.27$ keV and the central T_i rise was $\Delta T_{io} = 0.25$ keV from an initial value of $T_{io} = 0.86$ keV. The energy carried by the electron tail is small relative to the thermal plasma energy with $W_T = 0.19$ kJ and $W_B = (8.6 \rightarrow 11.3)$ kJ. The electron tail loss is negligible with $P_L = 0.05$ MW. However, the power lost due to collisional damping of LH ray trajectories at

the plasma periphery is significant with $P_{coll} = 0.27$ MW. The ohmic confinement time for this case is $\tau_E^{OH} = 19.2$ msec and the confinement time during RF injection is $\tau_E^{TOT} = 8.7$ msec [where $\tau_E^{TOT} = (W_B + W_T)/(P'_{oh} + P_{in})$ and P'_{oh} is the ohmic heating power during RF injection]. It is instructive to compare the magnitude of χ_e used for the LH heating simulation with the magnitude of χ_e used in the LH current driven discharges of Sec. VI B. From Eqs. 2(b) and (3) we see that χ_e at the plasma center is given by

$$\chi_{eo} = M_e \frac{C_\mu^{0.4} 1.6 \times 10^4}{n_{eo}} \frac{a B_\phi^{0.3} Z_{eff}^{0.2}}{R_o^{1.9} q_a^{0.6}}, \tag{38}$$

where $\chi_{eo} = \chi_{eo}(\mathrm{cm}^2/\mathrm{sec})$ and the other quantities are expressed in the same units as given after Eq. (3). If Eq. (38) is evaluated for the LH current driven discharges in the range $3 \times 10^{19}\,\mathrm{m}^{-3} \lesssim \bar{n}_e \lesssim 7 \times 10^{19}\,\mathrm{m}^{-3}$, one obtains $\chi_{eo} \simeq 3.1 \times 10^3\,\mathrm{cm}^2/\mathrm{sec}$. For the LH heated discharge, Eq. (38) yields $\chi_{eo} = 4.4 \times 10^3\,\mathrm{cm}^2/\mathrm{sec}$. Thus the magnitude of χ_{eo} at the plasma center is about 40% higher in the heating case at higher densities than in the cases with LHCD.

The ohmic and RF profiles of electron temperature are plotted in Fig. 11(a). The RF profile corresponds to 100 msec after the RF is turned on. The half-width for $T_e(r)$ actually decreases during RF injection from $\lambda_e = 8.9$ cm to $\lambda_e = 8.6$ cm. The loop voltage decreased from 1.75 V to 1.15 V. The radial profile of RF power deposition (at a time of $t_{rf} + 100$ msec) is shown in Fig. 11(b). The collisional absorption near $r = a$ is apparent with $P_{coll} = 0.27$ MW. The remaining RF power is absorbed via quasilinear electron Landau damping at $0 \lesssim r \lesssim 7$ cm. Figure 11(c) is the electron distribution function at a radial location of 4.54 cm (corresponding to the maximum in the RF deposition profile), plotted as a function of parallel kinetic energy. The narrow velocity extent of the plateaus in Fig. 11(c) is due to

the better defined RF power spectrum for the heating phasing ($\Delta\phi = 180°$) and is to be contrasted to the relatively wide plateaus found in the current drive and ramp up simulations (Figs. 6 and 10). The plateaus for $v_{\|} > 0$ and $v_{\|} < 0$ are nearly symmetric because of the bi-directional nature of the injected RF spectrum. In fact a small positive RF current ($\sim$ 20 kA) is generated because of the slight asymmetry in $F_e(r, v_{\|})$ caused by the DC electric field drift. The endpoints of the plateaus in Fig. 11(c) are in good agreement with the limit imposed by wave accessibility [$n_{\|acc} = 1.97$ and $E(n_{\|acc}) = 82$ keV] and the condition for strong quasilinear electron Landau damping [$n_{eld} \lesssim 5.7$ and $E(n_{eld}) \gtrsim 8$ keV]. In terms of $v_{\|}/v_e$, the plateau extent is from $v_1/v_e = 2.29$ to $v_2/v_e = 6.63$.

E. LHRF Sawtooth Stabilization Results

The current drive simulation model has been used to analyze LHRF sawtooth stabilization experiments performed on Alcator C.[7] Experimentally, sawteeth were found to be stablilized in discharges at $n_e \gtrsim 1.1 \times 10^{20} \mathrm{m}^{-3}$ and $B_\phi \approx 6.0$ T, by injecting RF power using a "current drive" waveguide phasing ($\Delta\phi = +90°$). Futhermore, complete stabilzation was only achieved for a certain range of injected RF powers, 0.5 MW $\lesssim P_{in} \lesssim$ 0.9 MW. Also, sawteeth were not observed to be stabilized using an "anti-current drive" ($\Delta\phi = -90°$) phasing or a "heating" phasing ($\Delta\phi = 180°$). By simulating these experiments, we shall show here that the resulting profiles of $\tilde{J}_{rf}$ and $J_{\|}$ yield profiles of q which are expected to be stable to the $m = 1$ mode.

The parameters used in these numerical studies were $a = 0.165\,\mathrm{m}, \mathrm{R_o} = 0.64\,\mathrm{m}$, $B_\phi = 6.2\,\mathrm{T}, \mathrm{I_p} = 260\,\mathrm{kA}, \bar{\mathrm{n}}_\mathrm{e} = 1.1 \times 10^{20}\,\mathrm{m}^{-3}, \mathrm{n_{eo}}/\bar{\mathrm{n}}_\mathrm{e} = 1.27, \mathrm{n_{ea}} = 0.15 \times \mathrm{n_{eo}}$, hydrogen gas, $M_i = 6$, relative waveguide phase $\Delta\phi = \pm 90°, \tau_L^{(\pm)} = \tau_o^{(\pm)}\gamma^3, \tau_o^{(\pm)} =$ 7.5 msec, $f_0 = 4.6$ GHz, $\Delta t_{rf} = 130$ msec, and $P_{in} = (0.4 - 1.4)$ MW. The electron

density was the same prescribed function used in the previous subsections. The voltage V_{OH} (t) was programmed so that $\dot{I}_p = 0$ (discharge was maintained at constant current).

An example for which sawtooth stabilization was achieved with $\Delta\phi = +90°$ and $P_{in} = 0.6$ MW is shown in Figure 12. A value of $M_e = 1.35$ resulted in an increase in T_{eo} from 1.3 keV to 1.75 keV and an increase in T_{io} from 0.86 keV to 1.12 keV. The corresponding plasma loop voltage decreased from 1.62 V to 1.01 V. The net RF current in this case was $\tilde{I}_{rf} = 33\,\mathrm{kA} \approx 0.1 \times \mathrm{I_p}$, with 54 kA of positive RF current and 21 kA of negative current. The radial profiles of $\tilde{J}_{rf}, J_{\|}$, and q are plotted in Figures 12(a) - 12(c). The ohmic plasma should be unstable to the m=1 mode since $q(0) < 1$ [Fig. 12(c)]. The radial position where $q(r) = 1$ is $r \equiv r_1 = 1.6$ cm for the ohmic plasma.

The profiles for the RF plasma are plotted at $t_{rf} + 3$ msec and $t_{rf} + 90$ msec. The profiles at $t_{rf} + 3$ msec are representative of the first $(10 - 15)$ msec during RF injection in that $q(r) > 1$ for $0 \leq r \leq a$ [see Figure 12(c)]. Initially a positive RF current density is generated at $r \simeq 2$ cm resulting in an increase in $J_{\|}$ at that point. The current density on-axis tends to decrease in order to conserve current, resulting in $q(0) > 1$. At later times, $t \gtrsim t_{rf} + 15$ msec, the parallel electric field (which is initially depressed at $0 \lesssim r \lesssim 4$ cm, due to the localized RF current generation at that point), tends to increase on-axis, as it diffuses radially outward. $J_{\|}(0)$ increases in response to this diffusion. However, a "shoulder" or flattened region is still maintained on $J_{\|}$ at $2\,\mathrm{cm} \lesssim \mathrm{r} \lesssim 4$ cm due to a positive RF current generation which is now localized radially in that region. This current pedestal or shoulder is also maintained to a lesser degree by a negative RF current density generated at $7\,\mathrm{cm} \lesssim \mathrm{r} \lesssim 10$ cm due to waves launched at $-6 \lesssim n_{\|} \lesssim -4$ in the injected Brambilla

spectrum. These high $n_{\|}$ waves tend to be absorbed far off axis and reduce $J_{\|}$ at that point. $J_{\|}$ then increases somewhat at $r < a/2$ in response to this reduction at $r > a/2$, in order to conserve the total current. The resulting profiles of $q(r)$ [Figure 12(c)] tend to be flat just outside of the radial position r_1', where $q(r_1') = 1$ for the RF plasma with $r_1' \simeq 1.3$ cm and $q(0) = 0.97$. As already mentioned, according to the numerical predictions of resistive and fully toroidal MHD codes [18], $q(r)$ profiles with $q(0) < 1$ and $dq(r)/dr \approx 0$ near r_1' have been found to be stable to the $m = 1$ mode. One point of disagreement between the present code results and the MHD code predictions is that $q(r)$ is flattened at $r \gtrsim r_1'$ in the LHCD code results, whereas the MHD code predictions [18] indicate that this flattening should occur at $r \lesssim r_1'$.

An interesting aspect of the Alcator C experiment which is explained by the model results in Figure 12 is the increase in the internal inductance (l_i) observed during stabilization ($\Delta\phi = +90°$). For the case in Figure 12, $l_i/2$ increased from 0.64 to 0.74 during RF injection. This increase in l_i is due to the pedestal in the $J_{\|}$ profile near the $q(r) = 1$ surface and due to the reduction in current density at $r \gtrsim 8$ cm. Finally we note that the bulk plasma energy increased from 7.45 kJ to 9.96 kJ during the RF pulse and β_θ^K increased from 0.35 to 0.47. The contribution to β_θ from energy stored in the electron tail is small with $W_T = 0.23$ kJ and $\beta_\theta^{TAIL}(a) = 0.013$. Also the electron tail and collisional losses were small with $P_L = 0.08$ MW and $P_{coll} = 0.06$ MW.

Simulation results obtained with "anti-current drive" phasing ($\Delta\phi = -90°$) and $P_{in} = 0.6$ MW are shown in Figure 13. Stabilization would not be expected in this case since $q(0) < 1$ and there is no evidence of a flattening of $q(r)$ near r_1' [see Figure 13(c)]. A significant, negative RF current is generated initially at $2\,\mathrm{cm} \lesssim r \lesssim 4$

cm and then later ($t_{rf} + 90$ msec) at $3\,\text{cm} \lesssim \text{r} \lesssim 7$ cm [Figure 13(a)]. This tends to reduce $J_\parallel$ at $(2-6)$ cm, causing $J_\parallel$ on-axis to remain near its ohmic value in order to conserve total current [see Figure 13(b)]. The resulting $q(r)$ profile has $q(0) < 1$ during the entire RF pulse and clearly no flattening of $q(r)$ can occur near the $q(r) = 1$ surface. The RF power in the injected spectrum, at high $n_\parallel$ ($4 \lesssim n_\parallel \lesssim 6$), is now launched in the "current-drive" direction and damps at $7\,\text{cm} \lesssim \text{r} \lesssim 10$ cm, generating a positive RF current in that region. The profile for $J_\parallel$ is then broader at $r > a/2$, leading to a slight decrease in $l_i/2$ from 0.65 to 0.63.

For the case in Figure 13, T_{eo} increased from 1.3 keV to 2.05 keV and the corresponding plasma loop voltage decreased from 1.62 V to 0.82 V. T_{io} increased from 0.86 keV to 1.18 keV. The net RF current was -9 kA, with 25 kA of positive RF current and 34 kA of negative RF current. Again the change in β_θ was mostly in β_θ^K which increased from 0.35 to 0.59, with W_B rising from 7.45 kJ to 12.7 kJ. The energy carried by the electron tail was 0.17 kJ and $\beta_\theta^{TAIL}(a) = 0.01$. The tail loss was somewhat higher for this phasing with $P_L = 0.12$ MW and the collisional absorption was again small with $P_{coll} = 0.04$ MW.

At RF powers of $P_{in} < 0.5$ MW, it is found that the RF current density generation off-axis near the $q = 1$ surface is not large enough to either reduce $J_\parallel(0)$ and raise $q(0)$ above unity or to create a pedestal on $J_\parallel$ near r_1' and therefore reduce $dq(r)/dr$ at that point. Consequently sawtooth stabilization would not be expected at $P_{in} < 0.5$ MW, in agreement with experiment.[7] At higher RF powers ($P_{in} \lesssim 1.3$ MW), stable current and q profiles continue to be found with $q(r) > 1$ for $0 \leq r \leq a$, during the entire RF pulse. This is only in partial agreement with experiment [7] where sawteeth were observed to be completely stabilized only up to RF powers of $P_{in} \lesssim 0.85$ MW and then were found to recur after a few tens of milliseconds into

the RF pulse at $P_{in} \gtrsim 0.9$ MW. Code results do indicate however, that at $P_{in} \geq 1.4$ MW, enough RF current is generated off-axis ($\tilde{I}_{rf} \simeq 75$kA) so that $(10 - 15)$ msec after the RF is turned on, a q profile develops in which the $q = 1$ surface occurs at two radial locations, with $q(0) > 1$ and the minimum value of $q \equiv q_{min} < 1$. This type of q profile should be unstable.

VIII. Summary and Conclusions

In this paper we have described a simulation model for LH current drive and heating. The model consists of a toroidal ray tracing calculation including multiple radial reflections of LH ray trajectories and a parallel velocity Fokker Planck calculation which includes the DC electric field and an arbitrary perpendicular velocity temperature due to pitch-angle scattering. The effect of finite electron tail confinement is modelled by a phenomenological loss of the form [17] $\tau_L^{(\pm)} = \tau_o^{(\pm)} \gamma^3$, in the Fokker Planck calculation. The radial transport of fast electrons is described by a model diffusion equation for the suprathermal RF current density. The source term, diffusion coefficient, and current destruction rate for this equation are estimated from the steady state Fokker Planck solution [Equation (14)]. A system of $1 - D$ radial transport equations and an evolution equation for ψ (the poloidal flux function) are then solved in conjunction with the Fokker Planck and wave propagation codes. The electron tail confinement parameter $\tau_o^{(\pm)}$ is fixed in the steady state LHCD by the requirement that $\tilde{I}_{rf} = I_p$, given some value of injected RF power (P_{in}). [The value of $\tau_o^{(\pm)}$ is not important at high density since $\tau_o^{(\pm)} \gg \tau_s$, i.e., electrons thermalize rapidly.] The magnitude of χ_e for the RF plasma is then adjusted to obtain the experimentally measured values of W_B and T_{eo}. It is therefore possible to determine the magnitude of the electron thermal transport during

LHCD and LHH which is consistent with both the theoretically predicted wave propagation/absorption and the experimentally measured stored energy and electron temperature.

Modelling of discharges maintained only by LH driven current at $I_p = 140$ kA, $3 \times 10^{19}\,\mathrm{m}^{-3} \leq \bar{n}_e \lesssim 7 \times 10^{13}\,\mathrm{m}^{-3}$, and $P_{in} = (0.3 - 1.0)$ MW, indicates that the experimental temperatures and stored energy are consistent with a χ_e whose magnitude is independent of n_e. The required value of RF current ($\tilde{I}_{rf} = 140$ kA) is found to be accurately predicted by taking $\tau_o^{(+)} = \tau_o^{(-)} = 3$ msec throughout this density range. At $\bar{n}_e \lesssim 3 \times 10^{19}\,\mathrm{m}^{-3}$, the resulting electron tail loss is significant with $P_L \lesssim 0.3 \times P_{in}$, whereas $P_L \approx 0.15 \times P_{in}$ at $\bar{n}_e = 7 \times 10^{19}\,\mathrm{m}^{-3}$. The energy stored in the electron tail is significant at $\bar{n}_e \lesssim 3 \times 10^{19}\,\mathrm{m}^{-3}$ with $W_T \gtrsim W_B \sim 1$ kJ. However at $\bar{n}_e = 7 \times 10^{19}\,\mathrm{m}^{-3}$, W_T is reduced relative to W_B with $W_T \simeq 0.3 \times W_B$. Because about 30% of the RF power is launched with $n_\parallel < 0$ [Figure 1(a)], negative RF current generation was found to be significant in these cases with $\tilde{I}_{rf}^{(-)} \approx (0.2 - 0.3) \times \tilde{I}_{rf}^{(+)}$. As in previous work [10] it was found that toroidally induced increases in $k_\parallel$ were sufficiently large so as to allow injected waves at high parallel phase velocity ($n_\parallel \lesssim 1.5$) to interact with electrons at $(2 - 3) \times v_e$ ($n_\parallel \gtrsim 5$), and thus populate the electron tail. Waves at $n_\parallel \lesssim 1.5$ were then able to Landau damp thus maintaining the electron plateau at high parallel phase velocity. The diffusion of fast electrons was an important effect at $\bar{n}_e \lesssim 3 \times 10^{19}\,\mathrm{m}^{-3}$ where centrally peaked profiles of "diffused" RF current density ($\tilde{J}_{rf}$) were found, although the RF deposition profiles were peaked off-axis at $r \simeq 0.25 \times a$ [see Figures 2(a) and 2(b)]. At high density ($\bar{n}_e \geq 7 \times 10^{19}\,\mathrm{m}^{-3}$) the diffusion of fast electrons was less of an effect because the electrons thermalized rapidly before spatially diffusing an appreciable distance. In this case the profiles of $\tilde{J}_{rf}$ and S_{rf} were similar.

The modelling of LH ramp up experiments in Alcator C indicated that in order to reproduce the experimentally measured values of conversion efficiency ($\bar{\eta}_{el}$) it was necessary to minimize the increase in negative RF current generation which occurred as $\bar{n}_e$ was lowered from $3 \times 10^{19}\,\mathrm{m}^{-3}$ to $1 \times 10^{19}\,\mathrm{m}^{-3}$. This was accomplished by decreasing $\tau_o^{(-)}$ from 3 msec to 0.5 msec, resulting in an increase in $\bar{\eta}_{el}$ from 0.05 to 0.135. The need to reduce $\tau_0^{(-)}$ is an uncertain point in the LH ramp up simulation since there are really no convincing experimental or theoretical reasons for doing this. It is worth pointing out however, that a similar assumption was made in Ref. [39] where the reverse runaway electrons were not confined at all in order to predict a ramp up efficiency in agreement with the PLT experiment.

Modelling results for LH heated discharges in Alcator C [7], at $\bar{n}_e \gtrsim 1.4 \times 10^{20}\,\mathrm{m}^{-3}$ and $B_\phi \geq 6$ T, indicate the importance of the power lost due to collisional damping of the injected LH waves at the plasma periphery, with $P_{coll} \approx 0.3 \times P_{in}$. The energy stored in the electron tail and the power lost due to finite electron tail confinement were both negligible at this density. In addition, the extent of the plateau in the electron distribution function for LHH was found to be narrow relative to the velocity extent of the electron tails in LHCD and LH ramp up [compare Figs. (6), (10), and 11(c)]. The magnitude of χ_e necessary to match the experimentally measured values of stored energy and T_{eo} was about 40% higher than the value required in the LH current driven discharges.

Finally, the simulation model was applied to LHRF sawtooth stabilization experiments in Alcator C. Code results indicated that for $\Delta\phi = 90°$ and $P_{in} \gtrsim 0.6$ MW, a pedestal or "shoulder" was formed on the $J_\parallel$ profile near the $q = 1$ surface, due to localized, positive RF current generation at that point. At RF powers of 0.6 MW $\lesssim P_{in} < 0.75$ MW, this current pedestal resulted in $q(r) > 1$ for $0 \leq r \leq a$

for the first $(10-15)$ msec of RF injection. At $t \gtrsim t_{rf}+15$ msec, the "shoulder" in $J_{\|}(r)$ resulted in a flattening of q near the $q=1$ surface with $q(0)<1$. This type of q profile is possibly stable to the $m=1$ mode according to the predictions [18] of resistive and fully toroidal MHD codes. At RF powers of 0.75 MW $\lesssim P_{in} \lesssim 1.3$ MW it was found that $q(r)>1$ for $0 \leq r \leq a$, throughout the RF pulse. At $P_{in} \gtrsim 1.4$ MW, enough RF current is generated to create a q profile with the $q=1$ surface occurring at two radial locations in the plasma [i.e., $q_{min}<1$ and $q(0)>1$]. This occurs about $(10-20)$ msec after the RF is turned on and might provide a qualitative explanation of why sawteeth recur in the experiment at high RF power and a few tens of milliseconds into the RF pulse. However, the RF power at which this is found in the code ($P_{in} \gtrsim 1.4$ MW) is higher than the threshold observed in the experiment ($P_{in} \gtrsim 0.90$ MW). At $P_{in}<0.6$ MW the RF current generation is not large enough to create a current pedestal that would result in a stable q profile. This power threshold for stabilization is in good agreement with experiment. For an "anti-current drive" phasing ($\Delta\phi=-90°$), q profiles are always found to have $q(0)<1$ and q monotically increasing with r. The negative RF current generation near the $q=1$ surface does not create a pedestal in the current density profile but rather tends to cause some peaking in $J_{\|}$. Thus the simulation model predicts profiles for $J_{\|}$ and q which are qualitatively in agreement with the results of sawtooth stabilization experiments in Alcator C.

In conclusion, a detailed simulation model for LHCD and LHH has been used to analyze the results of LHRF experiments in Alcator C. Such a model, when carefully applied, can provide valuable insight into the physics of LH wave propagation, absorption, and thermal and suprathermal electron energy transport during LHRF injection.

Acknowledgments:

We acknowledge the contributions of Dr. Ronald Englade to the development of this simulation model. We also acknowledge useful discussions with Dr. Catherine Fiore, Dr. Stephen Wolfe, and Professor Bruno Coppi. This work was supported by the US Department of Energy under contract No. DE-AC02-78ET51013.

Figure Captions:

Figure 1. Four waveguide, RF power spectra for Alcator C. (a) Relative waveguide phase $\Delta\phi = 90°$. (b) $\Delta\phi = 180°$. (From Ref. [36])

Figure 2. LHCD model results for Alcator C parameters of Sec. VI B ($\bar{n}_e = 3 \times 10^{19}\,\mathrm{m}^{-3}$ and $P_{in} = 0.32$ MW). (a) Radial profile of RF power density. (b) Radial profile of diffused RF current density. Profiles correspond to a time of $t_{rf} = 100$ msec where t_{rf} is the RF turn-on time.

Figure 3. LHCD model results for Alcator C parameters of Sec. VI B ($\bar{n}_e = 3 \times 10^{19}\,\mathrm{m}^{-3}$ and $P_{in} = 0.95$ MW). (a) Radial profile of RF power density. (b) Radial profile of diffused RF current density. Profiles correspond to a time of $t_{rf} + 100$ msec, where t_{rf} is the RF turn-on time.

Figure 4. LHCD model results for Alcator C parameters of Sec. VI B ($\bar{n}_e = 3 \times 10^{19}\,\mathrm{m}^{-3}$ and $P_{in} = 0.32$ MW). (a) Radial profiles of electron temperature. (b) Radial profiles of parallel electric field. Curves labelled OH and T_1 refer respectively to times of $t_{rf} - 5$ msec and $t_{rf} + 100$msec, where t_{rf} is the RF turn-on time.

Figure 5. LHCD model results for Alcator C parameters of Sec. VI B ($\bar{n}_e = 3 \times 10^{19}\,\mathrm{m}^{-3}$ and $P_{in} = 0.32$ MW). (a) Time behavior of plasma loop voltage. (b) Time behavior of total plasma current (I_p) and radially integrated RF current ($\tilde{I}_{rf}$).

Figure 6. LHCD model results for Alcator C parameters of Sec. VI B ($\bar{n}_e = 3 \times 10^{19}\,\mathrm{m}^{-3}$ and $P_{in} = 0.32$ MW). Electron distribution function at a radial location $r = 2.89$ cm versus parallel kinetic energy.

Figure 7. Ray trajectory for LHCD model example of Sec. VI B ($\bar{n}_e = 3 \times 10^{19}\,\mathrm{m}^{-3}$ and $P_{in} = 0.32$ MW). (a) Projection of the ray trajectory in the poloidal

cross-section of the tokamak. (b) Variation in ρ/a versus toroidal angle (ϕ). (c) Variation in the poloidal mode number (m) versus toroidal angle (ϕ). (d) Variation in parallel refractive index ($n_{\|}$) versus toroidal angle (ϕ). Initially $n_{\|} = 1.594$. (e) Normalized wave amplitude (P_N) that results from damping on quasilinear electron distribution ($n_{\|} > 0$), versus toroidal angle (ϕ).

Figure 8. LH ramp up model results for Alcator C parameters of Sec. VI C ($\bar{n}_e = 1 \times 10^{19}\,\mathrm{m}^{-3}$ and $P_{in} = 0.4$ MW). (a) Radial profile of diffused RF current density. (b) Radial profile of parallel electric field. Curves labelled OH and T_1 refer respectively to times of $t_{rf} - 5$ msec and $t_{rf} + 150$ msec, where t_{rf} is the RF turn-on time.

Figure 9. LH ramp up model results for Alcator C parameters of Sec. VI C ($\bar{n}_e = 1 \times 10^{19}\,\mathrm{m}^{-3}$ and $P_{in} = 0.4$ MW). (a) Time behavior of plasma loop voltage. (b) Time behavior of total plasma current (I_p) and radially integrated RF current ($\tilde{I}_{rf}$). (c) Time behavior of conversion efficiency ($\tilde{\eta}_{el}$).

Figure 10. LH ramp up model results for Alcator C parameters of Sec. VI C ($\bar{n}_e = 1 \times 10^{19}\,\mathrm{m}^{-3}$ and $P_{in} = 0.4$ MW). Electron distribution function at a radial location $r = 4.95$ cm versus parallel kinetic energy.

Figure 11. LHH model results for Alcator C parameters of Sec. VI D ($\bar{n}_e = 1.4 \times 10^{20}\,\mathrm{m}^{-3}$, $B_\phi = 5.5$ T, and $P_{in} = 1.0$ MW). (a) Radial profiles of electron temperature. (b) Radial profile of RF power density. Curves labelled OH and T_1 refer respectively to times of $t_{rf} - 5$ msec and $t_{rf} + 100$ msec, where t_{rf} is the RF turn-on time. (c) Electron distribution function at a radial location $r = 4.54$ cm versus parallel kinetic energy.

Figure 12. LHRF sawtooth stabilization model results for Alcator C parameters of Sec. VI E

($\bar{n}_e = 1.1 \times 10^{20}\,\mathrm{m}^{-3}$, $B_\phi = 6.2$ T, $\Delta\phi = +90°$, and $P_{in} = 0.6$ MW). (a) Radial profiles of diffused RF current density. (b) Radial profiles of toroidal current density. (c) Radial profiles of the safety factor for $0 \leq r \leq 5$ cm. Curves labelled OH, T_1, and T_2 refer respectively to times of $t_{rf} - 5$ msec, $t_{rf} + 3$ msec, and $t_{rf} + 90$ msec, where t_{rf} is the RF turn-on time.

Figure 13. LHRF sawtooth stabilization model results for Alcator C parameters of Sec. VI E ($\bar{n}_e = 1.1 \times 10^{20}\,\mathrm{m}^{-3}$, $B_\phi = 6.2$ T, $\Delta\phi = -90°$, and $P_{in} = 0.6$ MW). (a) Radial profiles of diffused RF current density. (b) Radial profiles of toroidal current density. (c) Radial profiles of the safety factor for $0 \leq r \leq 5$ cm. Curves labelled OH, T_1, and T_2 refer respectively to times of $t_{rf} - 5$ msec, $t_{rf} + 3$ msec, and $t_{rf} + 90$ msec, where t_{rf} is the RF turn-on time.

Table I: Density Scan for Ohmic Plasma ($B_\phi = 8$ T)

$\bar{n}_e(10^{19}\mathrm{m}^{-3})$	W_B (kJ)	P_{oh} (MW)	β_θ^K(a)	τ_E^{OH}(msec)
3	1.11	0.19	0.19	5.7
5.5	1.96	0.21	0.33	9.3
7	2.41	0.23	0.41	10.6

Table II: Density Scan for Steady State LHCD (RF Plasma)

$\bar{n}_e(10^{19}\mathrm{m}^{-3})$	W_B(kJ)	W_T(kJ)	$\tau_o^{(\pm)}$(msec)	M_e	τ_E^{TOT}(msec)	$\beta_\theta^K(a)$	$\beta_\theta^{TAIL}(a)$
3	1.19	1.00	3.0	0.95	6.8	0.19	0.21
5.5	2.43	1.12	3.0	1.75	5.5	0.38	0.22
7	3.38	1.21	3.0	2.10	4.8	0.53	0.24

Table III: Density Scan for Steady State LHCD (RF Plasma)

$\bar{n}_e(10^{19}\mathrm{m}^{-3})$	P_{in}(MW)	$\tilde{\eta}(A/W/m^2)$	P_L(MW)	P_{coll}(MW)	P_D(MW)
3	0.32	0.084	0.093	0.015	0.192
5.5	0.65	0.076	0.120	0.078	0.408
7	0.95	0.066	0.152	0.131	0.598

Table IV: Density Scan for LH Ramp Up

$\bar{n}_e(10^{19}\mathrm{m}^{-3})$	$\tau_0^{(+)}$(msec)	$\tau_o^{(-)}$(msec)	P_{in}(MW)	η_{el}	$\dot{I}_p$(kA/s)	$\tilde{I}_{rf}^{(+)}$(kA)	$\tilde{I}_{rf}^{(-)}$(kA)	M_e	Z_{eff}	v_{ph}/v_r
1	4	0.5	0.4	0.135	314	222	52	0.48	3	0.65
2	4	1	0.4	0.075	193	187	45	1.1	2.25	0.37
3	3	3	0.46	0.055	136	210	65	1.44	1.50	0.25

REFERENCES

[1.] YAMAMOTO, T., IMAI, T., SHIMADA, M., SUZUKI, N., MAENO,M., KONOSHIMA,S., FUJII,T., UEHARA,K., NAGASHIMA,T., FUNAHASHI,A., and FUJISAWA,N., Phys. Rev. Lett. **45**, 716 (1980).

[2.] LUCKHARDT,S. C., PORKOLAB,M., KNOWLTON,S. F., CHEN,K. -I., FISHER,A. S., MCDERMOTT,F. S., and MAYBERRY,M., Phys. Rev. Lett. **48**, 152 (1980).

[3.] BERNABEI,S., DAUGHNEY,C., EFTHIMION,P., HOOKE,W., HOSEA,J., JOBES,F., MARTIN,A., MAZZUCATO,E., MESERVEY,E., MOTLEY,R., STEVENS,J., VON GOELER,S., and WILSON,R., Phys. Rev. Lett. **49**, 1255 (1982).

[4.] PORKOLAB,M., SCHUSS,J. J., LLOYD,B., TAKASE,Y., TEXTER,S., BONOLI,P. T., FIORE,C., GANDY,R., GWINN,D., LIPSCHULTZ,B., MARMAR,E., PAPPAS,D., PARKER,R., and PRIBYL,P., Phys. Rev. Lett. **53**, 450 (1984).

[5.] GORMEZANO,C. C., BIBET,P., BLANC,P., BRIAND,P., BRIFFORD,G., CLEMET,M., GRELOT, P., HESS,W., ICHTCHENKO,G., MELIN,G., MOULIN,B., PANZARELLA,A., PARLANGE,F., POROT,E., REY,G. TAQUET,B., TERNEAY,F., VAN HOUTTE,D., in *Proceedings of the Eleventh European Conference on Controlled Fusion and Plasma Physics*, edited by S. Methfessel and G. Thomas, (European Physical Society, Petit-Lancy, Switzerland, 1983). Vol. I, p. 325.

[6.] SÖLDNER,F. X., MCCORMICK,K., ECKHARTT,D., KORNHERR,M., LEUTERER,F., BARTIROMO,R., BECKER,G., BOSCH,H. S., BROCKEN,H., DERFLER,H., EBERHAGEN,A., FUSSMANN,G., GEHRE,O., GERNHARDT,J., GIERKE,G.V., GIULIANA,A., GLOCK,E., GRUBER,O., HAAS,G., HESSE,M., HOFMANN,J., IZVOZCHIKOV,A., JANESCHITZ,G., KARGER,F., KEILHACKER,M., KLÜBER,O., LACKNER,K., LENOCI,M., LISITANO,G., MAST,F., MAYER,H. M., MEISEL,D., MERTENS,V., MÜLLER,E. R., MÜNICH,M., MURMANN,H., NIEDERMEYER,H., PIETRZYK,A., POSCHENRIEDER,W., RAPP,H., RIEDLER,H., RÖHR,H., RYTER,F., SCHMITTER,K. H., SCHNEIDER,F., SETZENSACK,C., SILLER,G., SMEULDERS,P., SPETH,E., STEUER,K. -H., VIEN,T., VOLLMER,O., WAGNER,F., WOYNA,F. V., and ZASCHE,D., Phys. Rev. Lett. **57**, 1137 (1987).

[7.] PORKOLAB,M., KNOWLTON,S., TAKASE,Y., TEXTER,S., BONOLI,P., FIORE,C., GOMEZ,C., GRANETZ,R., GWINN,D., MCDERMOTT,S., TERRY,J., in *Proceedings of the Thirteenth Conference on Controlled Fusion and Plasma Heating*, edited by G. Briffod and M. Kaufmann, (European Physical Society, Switzerland, 1986), Vol. II, p.445; KNOWLTON, S., et al., submitted to Nucl. Fusion.

[8.] PORKOLAB,M., LLOYD,B., TAKASE, Y., BONOLI,P., FIORE,C., GANDY,R., GRANETZ, R., GRIFFIN, D., GWINN,D., LIPSCHULTZ,B., MARMAR,E., MCCOOL, S., PACHTMAN, A., PAPPAS,D., PARKER,R., PRIBYL,P., RICE, J., TERRY, J., TEXTER, S., WATTERSON, R., and WOLFE, S., Phys. Rev. Lett. **53**, 1229 (1984).

[9.] ENGLADE,R. and BONOLI,P. T., in *Radiofrequency Plasma Heating*, edited by D. G. Swanson (American Institute of Physics, New York, 1985) p. 151.

[10.] BONOLI,P. T. and ENGLADE,R. C., Phys. Fluids **29**, 2937 (1986).

[11.] BONOLI,P. T., in *Proceedings of the Seventh APS Topical Conference on Applications of Radiofrequency Power to Plasmas*, (AIP, New York, 1987), paper A1.

[12.] VALEO,E. J., and EDER,D. C., Journal of Computational Physics **69**, 341 (1987).

[13.] TEXTER,S., KNOWLTON,S., PORKOLAB,M., TAKASE,Y., Nucl. Fusion **26**, 1279 (1986).

[14.] KNOWLTON,S., PORKOLAB,M., TAKASE,Y., TEXTER,S., BONOLI,P., FIORE,C., MCCOOL,S., MCDERMOTT,F. S., TERRY,J. L., Phys. Rev. Lett. **57**, 587 (1986).

[15.] TAKASE,Y., BONOLI,P., KNOWLTON,S., PORKOLAB,M., TEXTER,S., FIORE,C., MCCOOL,S., MCDERMOTT,S., TERRY,J., Nucl. Fusion **27**, 53 (1986).

[16.] TAKASE,Y., KNOWLTON,S., PORKOLAB,M., Phys. Fluids **30**, 1169 (1987).

[17.] MYNICK,H. E. and STRACHAN,J. D., Phys. Fluids **24**, 695 (1981).

[18.] HENDER,T. C., ROBINSON,D. C., SNIPES,J. A., *Proceedings of the Eleventh International Conference on Plasma Physics and Controllled Nuclear Fusion Research* (Kyoto, 1986) IAEA-CN-47/A-V-3.

[19.] ANTONSEN,T., COPPI,B., and ENGLADE,R., Nucl. Fusion **19**, 641 (1979).

[20.] HINTON,F. L., and HAZELTINE,R. D., Rev. Mod. Phys. **48**, 239 (1976).

[21.] TANG,W. M., Nucl. Fusion **26**, 1605 (1986).

[22.] COPPI,B., Comments Plasma Phys. Cont. Fusion **5**, 261 (1980).

[23.] COPPI,B., Fizica Plazmy **2**, 83 (1985).

[24.] KARNEY,C. F. F. and FISCH,N. J., Phys. Fluids **22**, 1817 (1979).

[25.] KENNEL,C. F. and ENGELMANN,F., Phys. Fluids **9**, 2377 (1966).

[26.] TRUBNIKOV,B. A., in *Reviews of Plasma Physics*, edited by M. A. Leontovich (Consultants Bureau, New York, 1970), Vol. I, p. 105.

[27.] HIZANIDIS,K., and BERS,A., Phys. Fluids **27**, 2673 (1984).

[28.] HEWETT,D., HIZANIDIS,K., KRAPCHEV,V., and BERS,A., in *Proceedings of the IAEA Technical Committee Meeting on Non-Inductive Current Drive in Tokamaks*, edited by D. F. H. Start, [Euratom/UKAEA Association, CLM-CD (1983)], Vol. II, p. 124.

[29.] FUCHS,V., CAIRNS,R. A., SHOUCRI,M. M., HIZANIDIS,K., and BERS,A., Phys. Fluids **28**, 3619 (1985).

[30.] MONDELLI,A., and OTT,E., Phys. Fluids **17**, 1017 (1974).

[31.] WEINBERG,S., Phys. Rev. **126**, 1899 (1962).

[32.] WERSINGER,J. M., OTT,E., and FINN,J. M., Phys. Fluids **21**, 2263 (1978).

[33.] STIX,T. H., *Theory of Plasma Waves*, (Mc-Graw Hill, New York, 1962).

[34.] SHAFRANOV, V. D., in *Reviews of Plasma Physics*, edited by M. A. Leontovich (Consultants Bureau, New York, 1966) Vol. 2, p. 103.

[35.] BRAMBILLA,M., Nucl. Fusion **16**, 47 (1976).

[36.] PORKOLAB, M., SCHUSS, J. J., LLOYD, B., TAKASE, Y., TEXTER, S., WATTERSON, R., BONOLI, P., ENGLADE, R., FIORE, C., GANDY, R., GRANETZ, R., GREENWALD, M., GWINN, D., LIPSCHULTZ, B., MARMAR, E., McCOOL, S., PAPPAS, D., PARKER, R., PRIBYL, P., RICE, J., TERRY, J., WOLFE, S., SLUSHER, R., SURKO, C., *Proceedings of the Fifth Topical Conference on Radiofrequency Plasma Heating* (Madison, 1983) p.88.

[37.] BRAMBILLA, M., in *Physics of Plasmas Close to Thermonuclear Conditions* (CEC, 1980) Vol. I 291.

[38.] PORKOLAB, M., in *Fusion* edited by E. Teller (Academic, New York, 1981) Vol. IB, Chap. 13, 151.

[39.] FISCH, N. J., and KARNEY, C. F. F., Phys. Rev. Lett. **54**, 897 (1985).

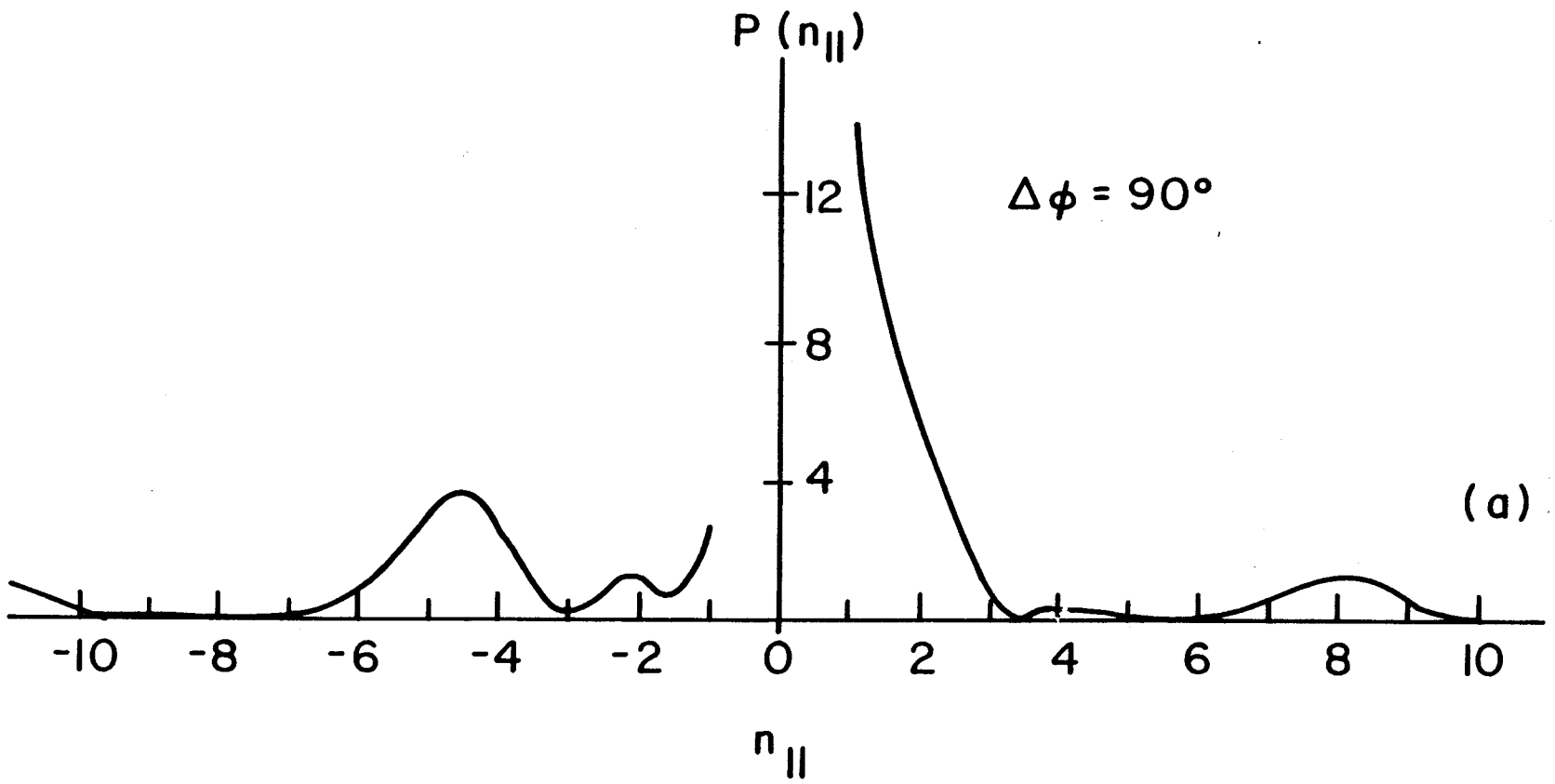

Fig. 1(a)

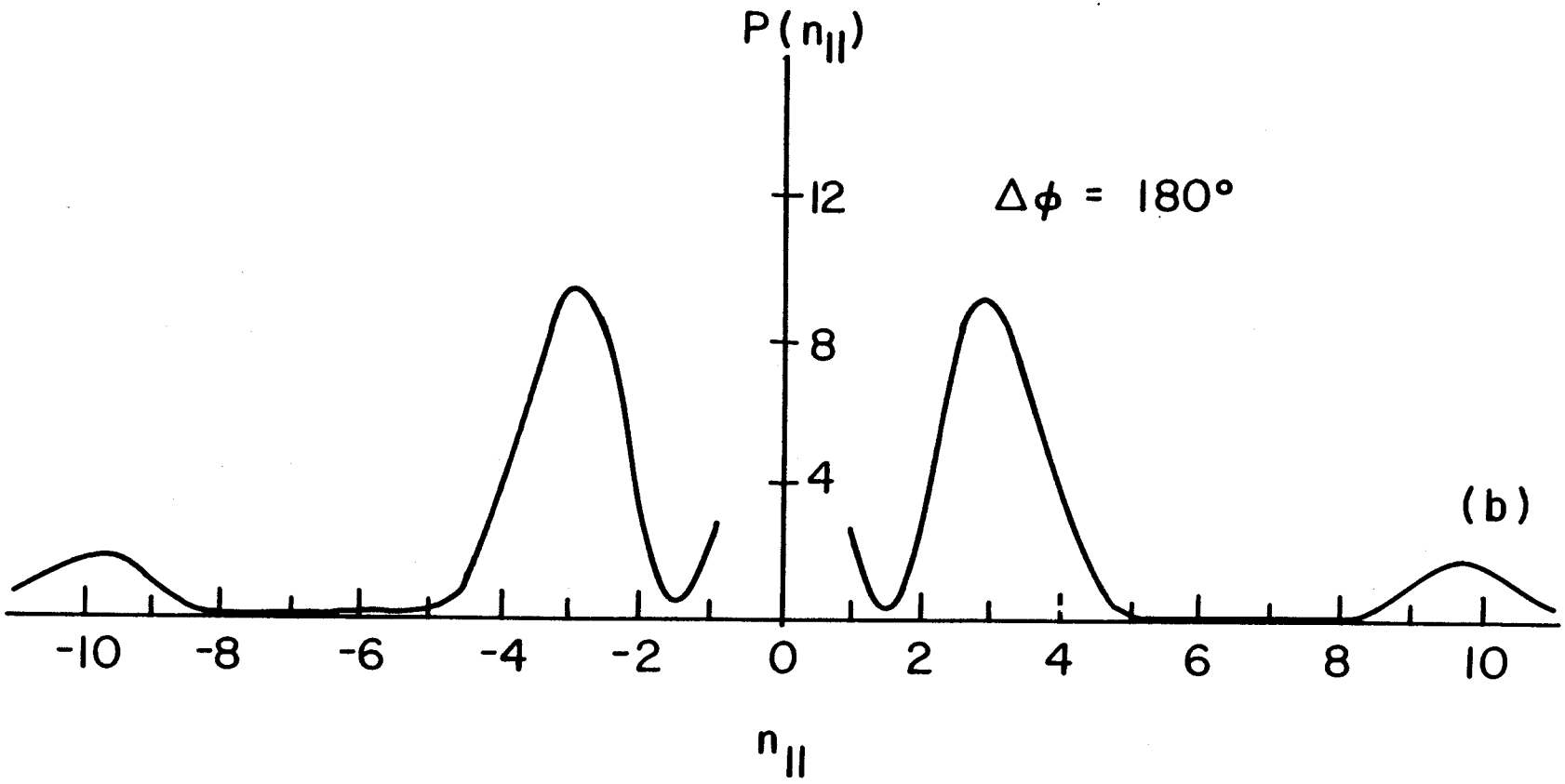

Fig. 1(b)

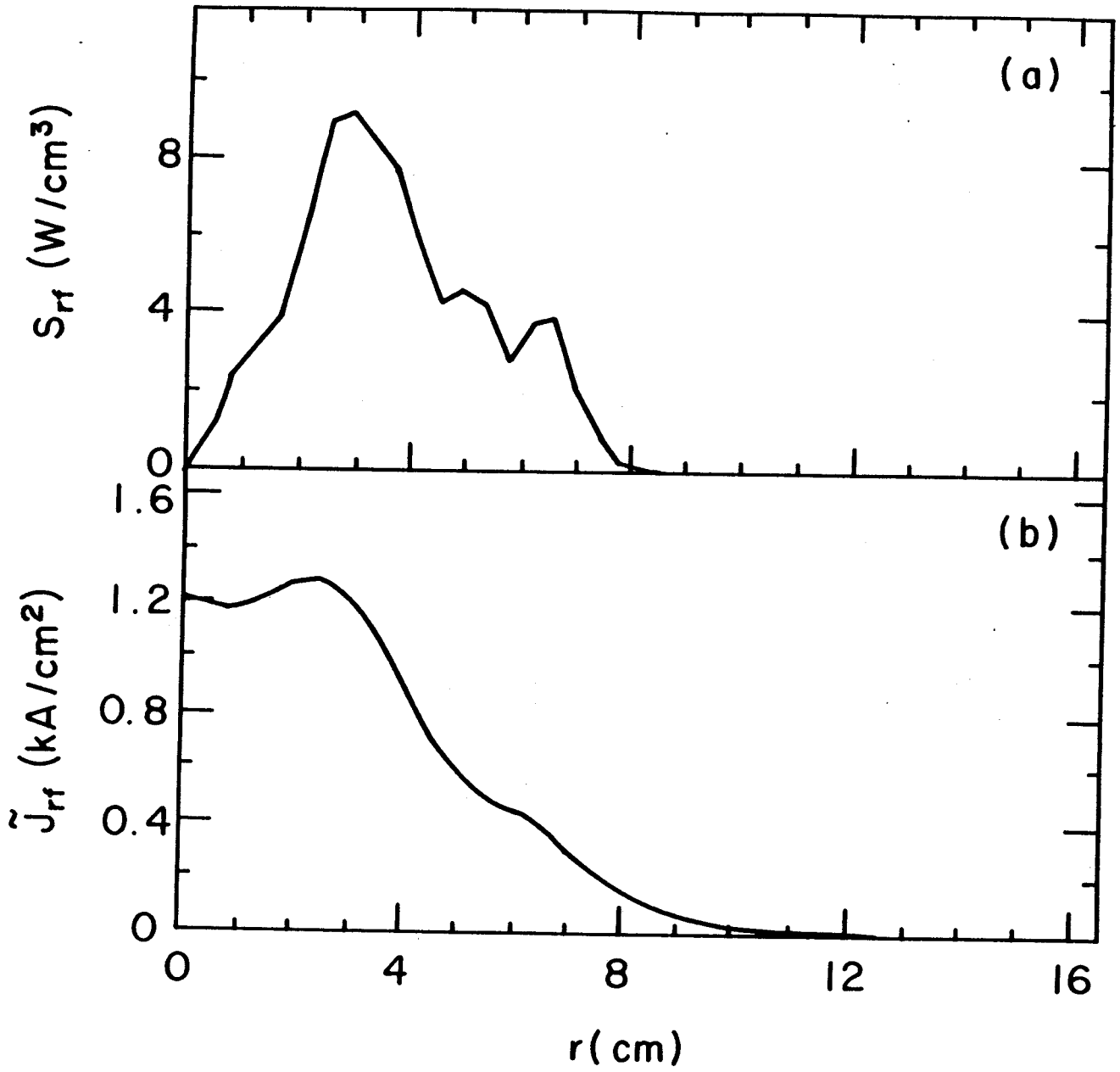

Fig. 2

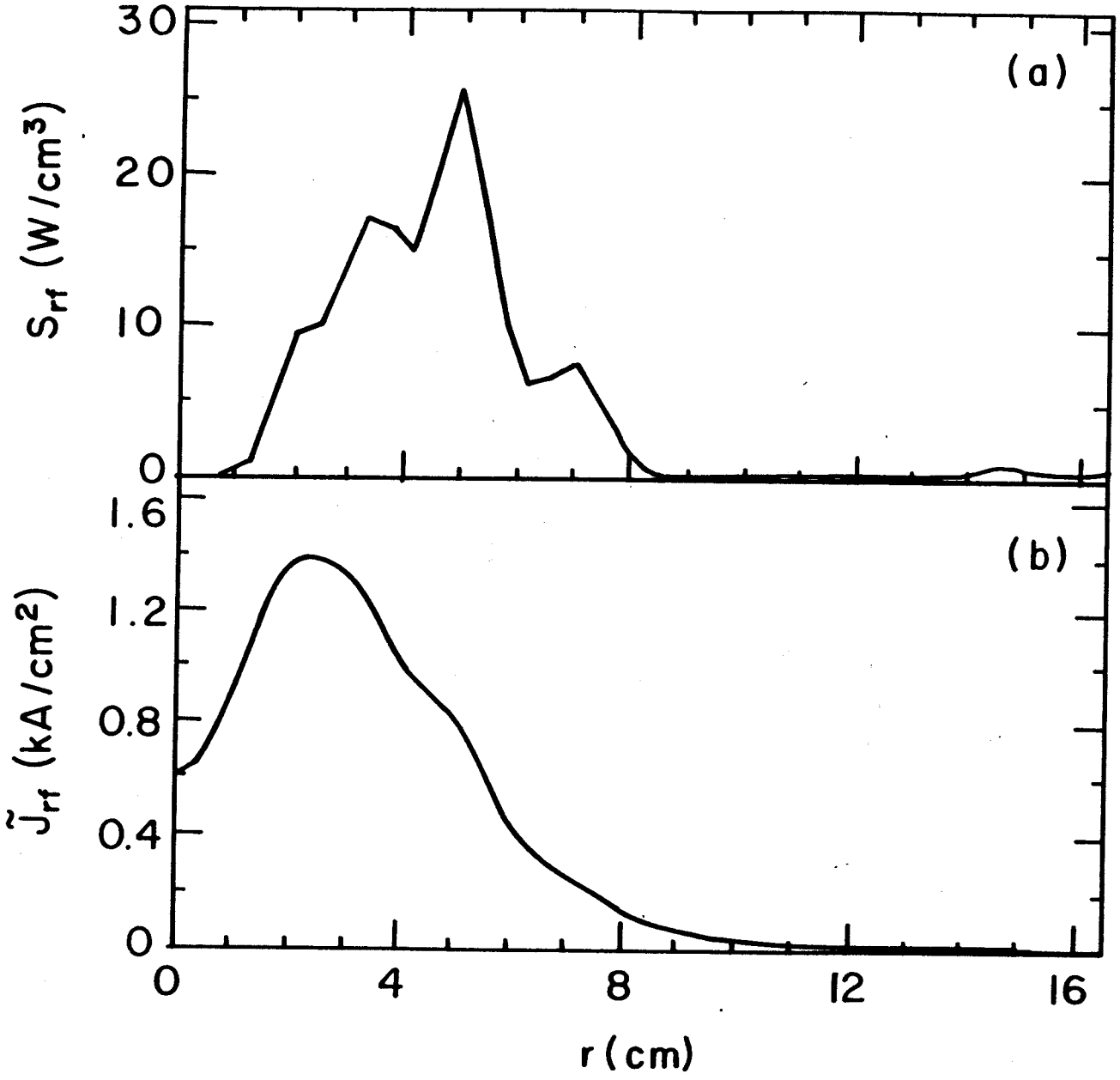

Fig. 3

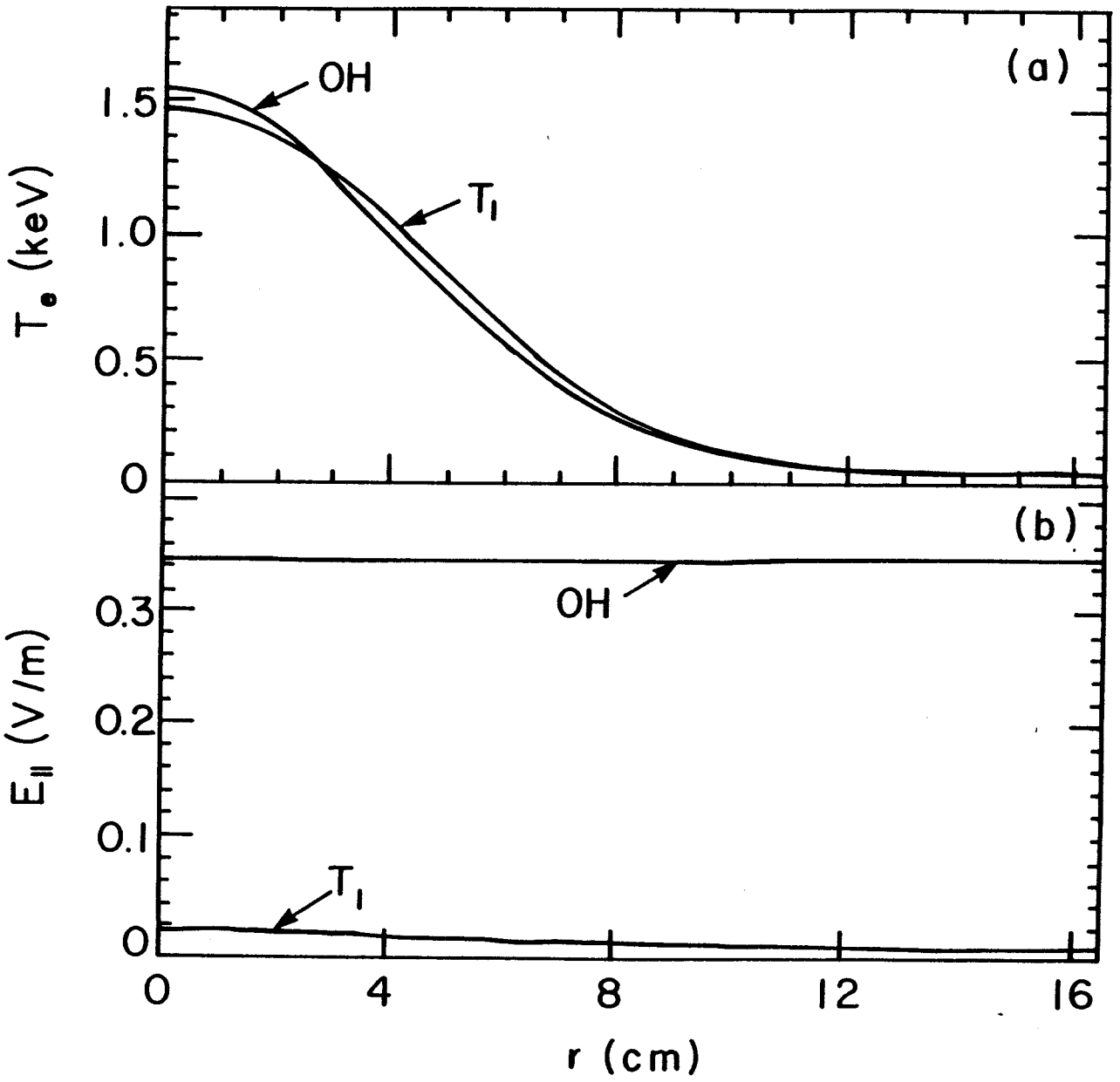

Fig. 4

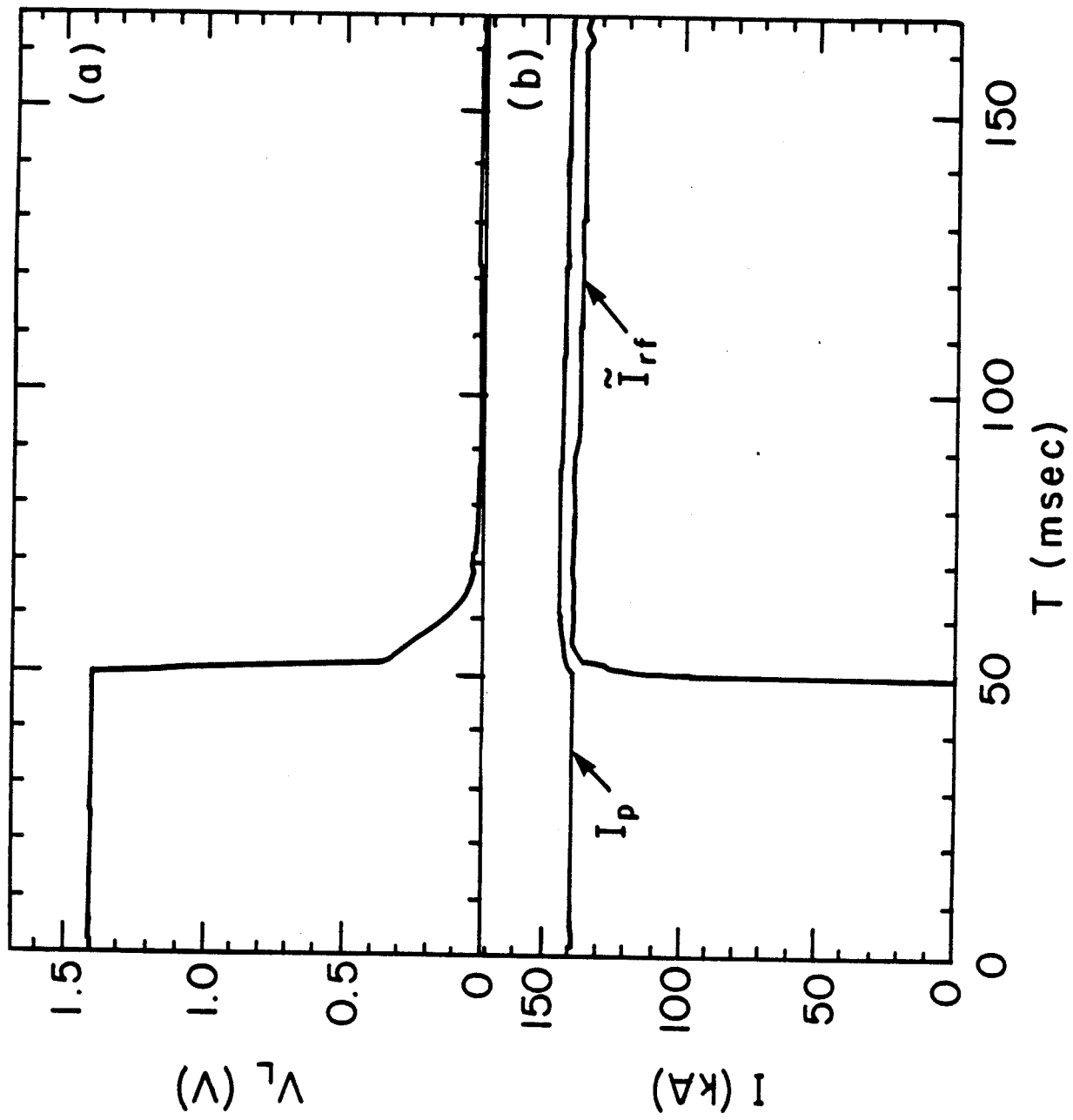

Fig. 5

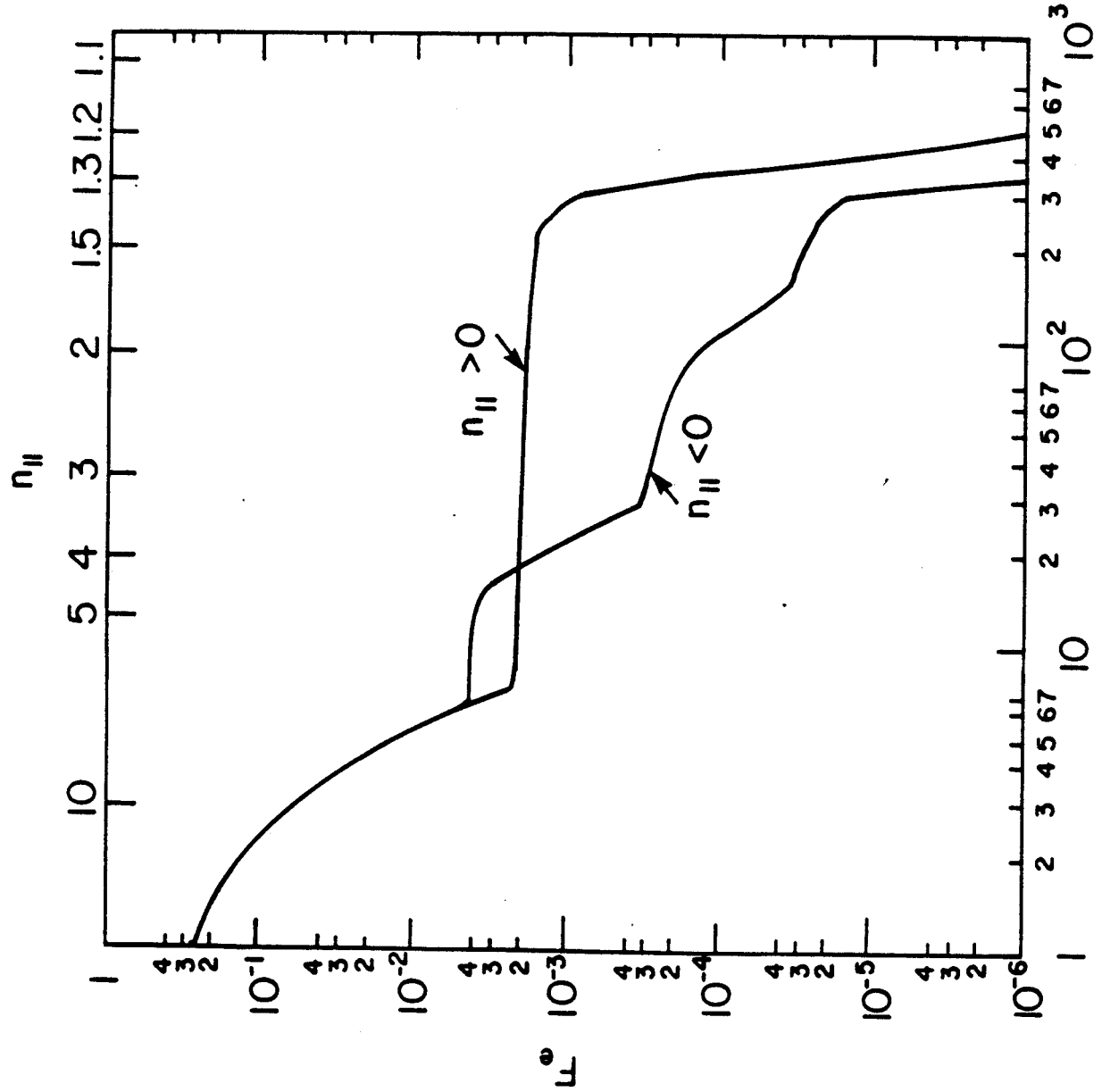
$n_{||}$
10
5
4
3
2
1.5
1.3
1.2
1.1
1
$n_{||} > 0$
$n_{||} < 0$
F_e
10^{-1}
10^{-2}
10^{-3}
10^{-4}
10^{-5}
10^{-6}
E (keV)
10
10^2
10^3

Fig. 6

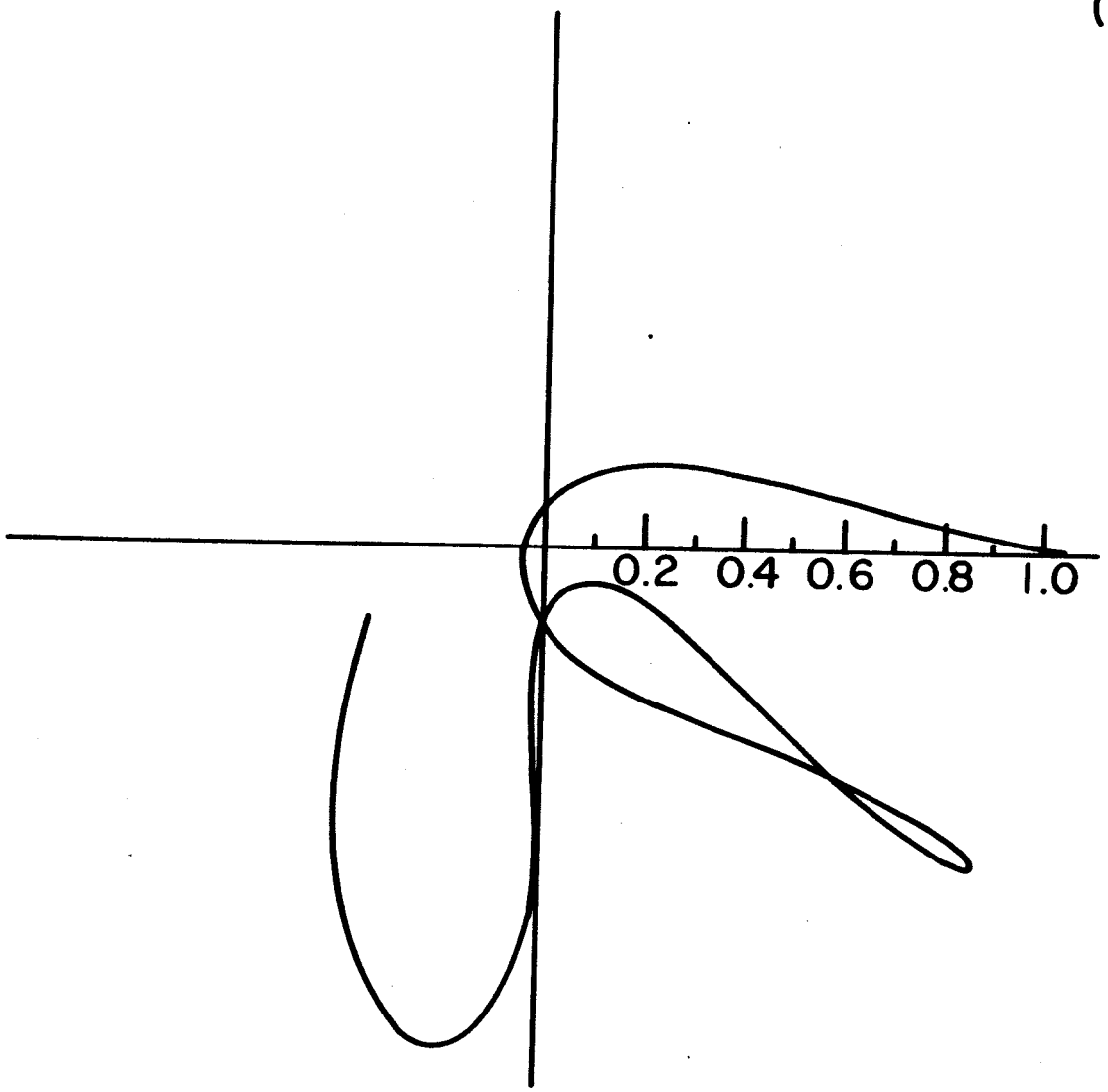

Fig. 7(a)

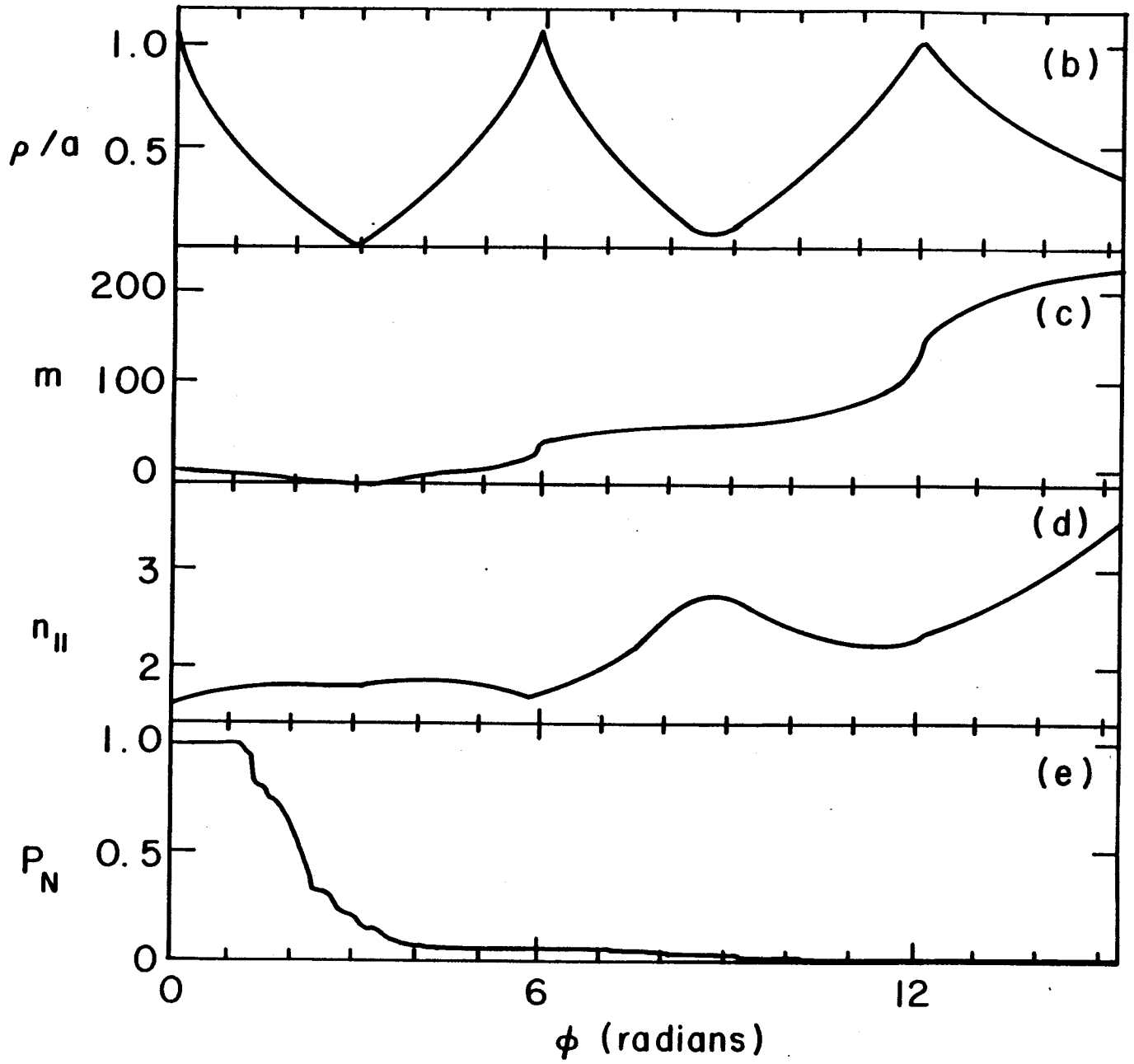

Fig. 7(b - e)

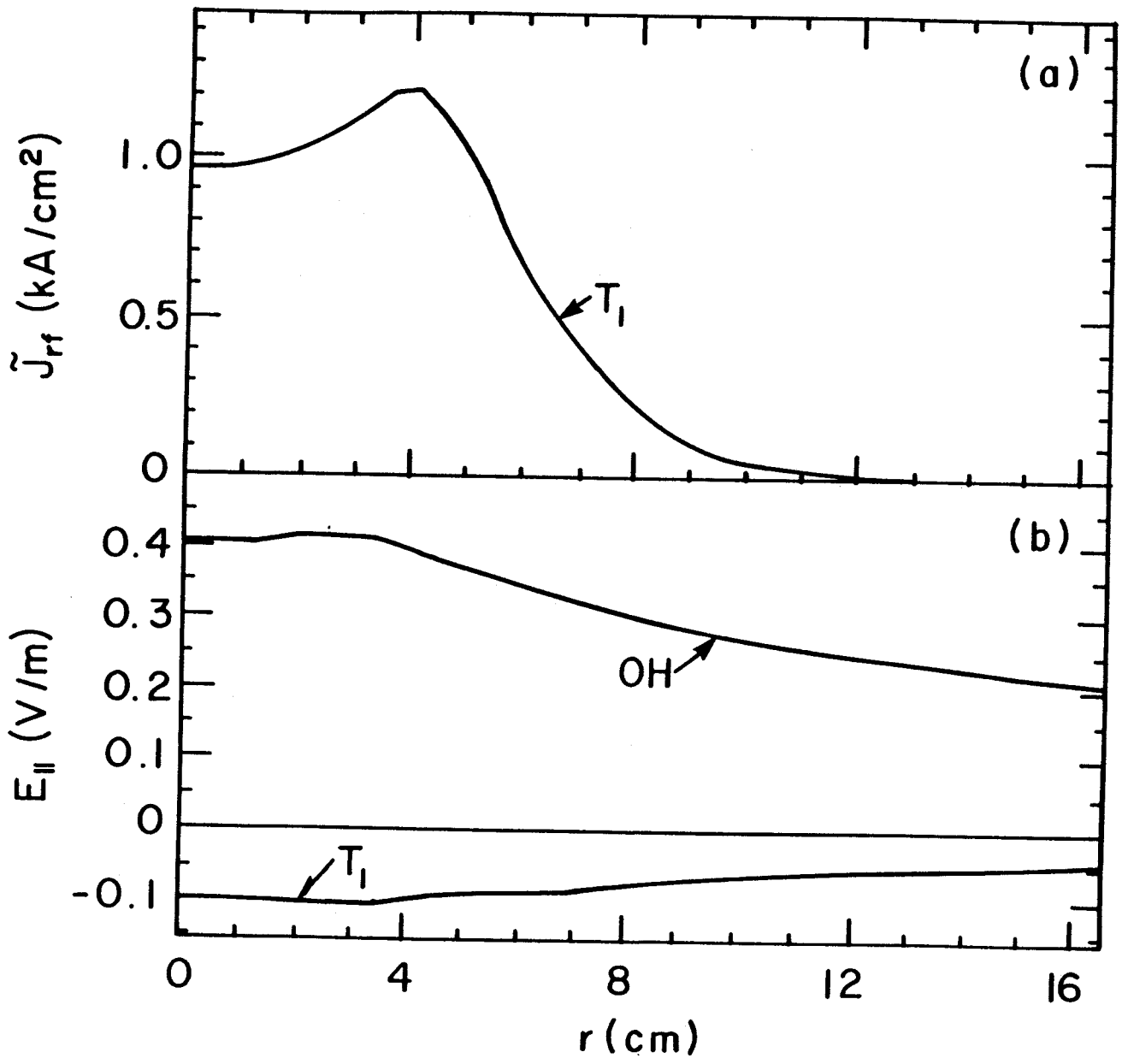
(a)
1.0
0.5
0
$\tilde{J}_{rf}$ (kA/cm²)
T_1
(b)
0.4
0.3
0.2
0.1
0
-0.1
$E_{\parallel}$ (V/m)
OH
T_1
0
4
8
12
16
r (cm)

Fig. 8

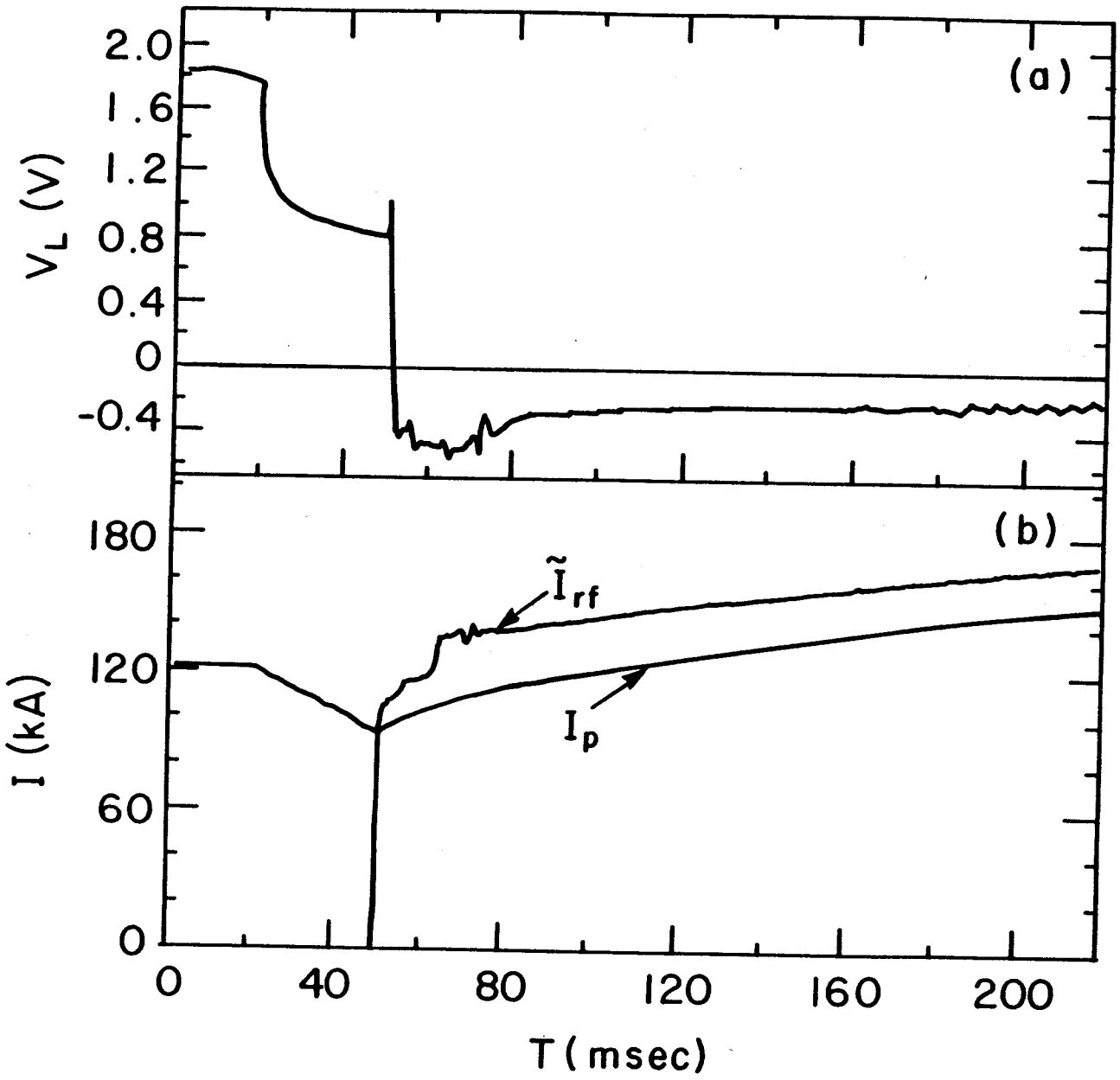
2.0
1.6
1.2
0.8
0.4
0
-0.4
V_L (V)
(a)
180
120
60
0
I (kA)
(b)
$\tilde{I}_{rf}$
I_p
0
40
80
120
160
200
T (msec)

Fig. 9(a,b)

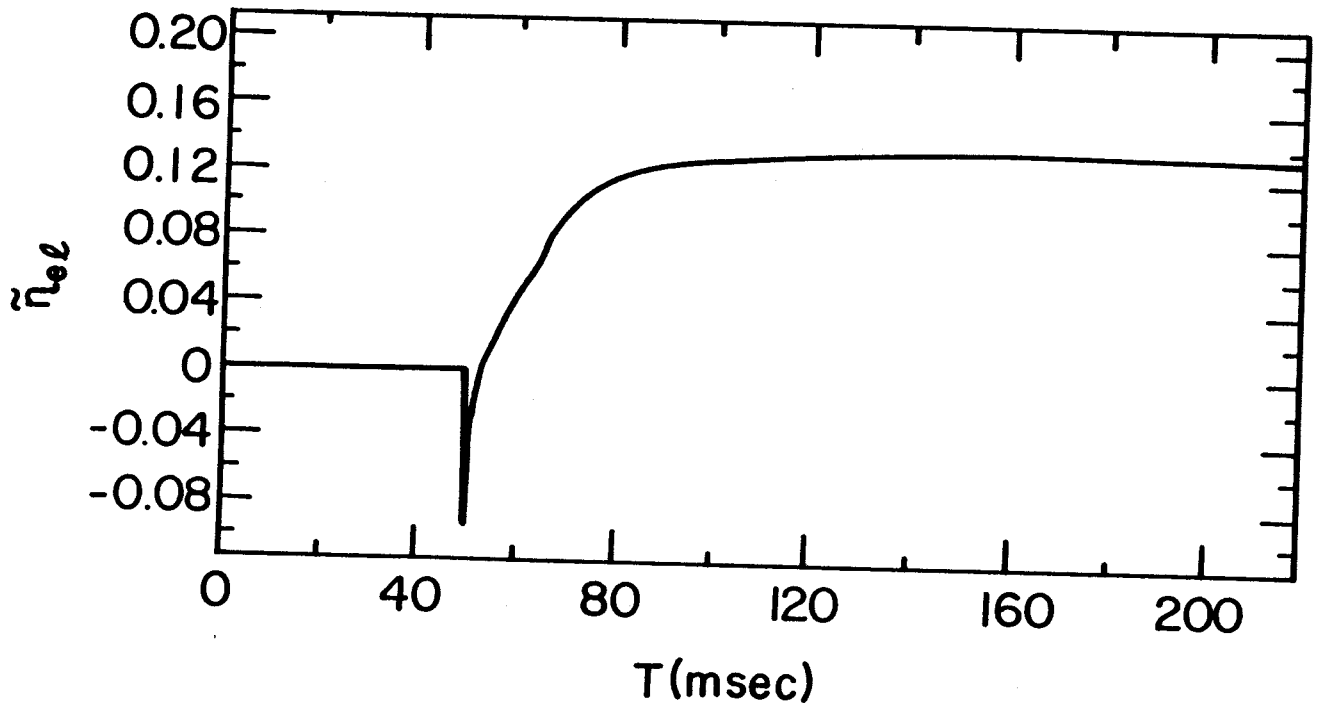

Fig. 9(c)

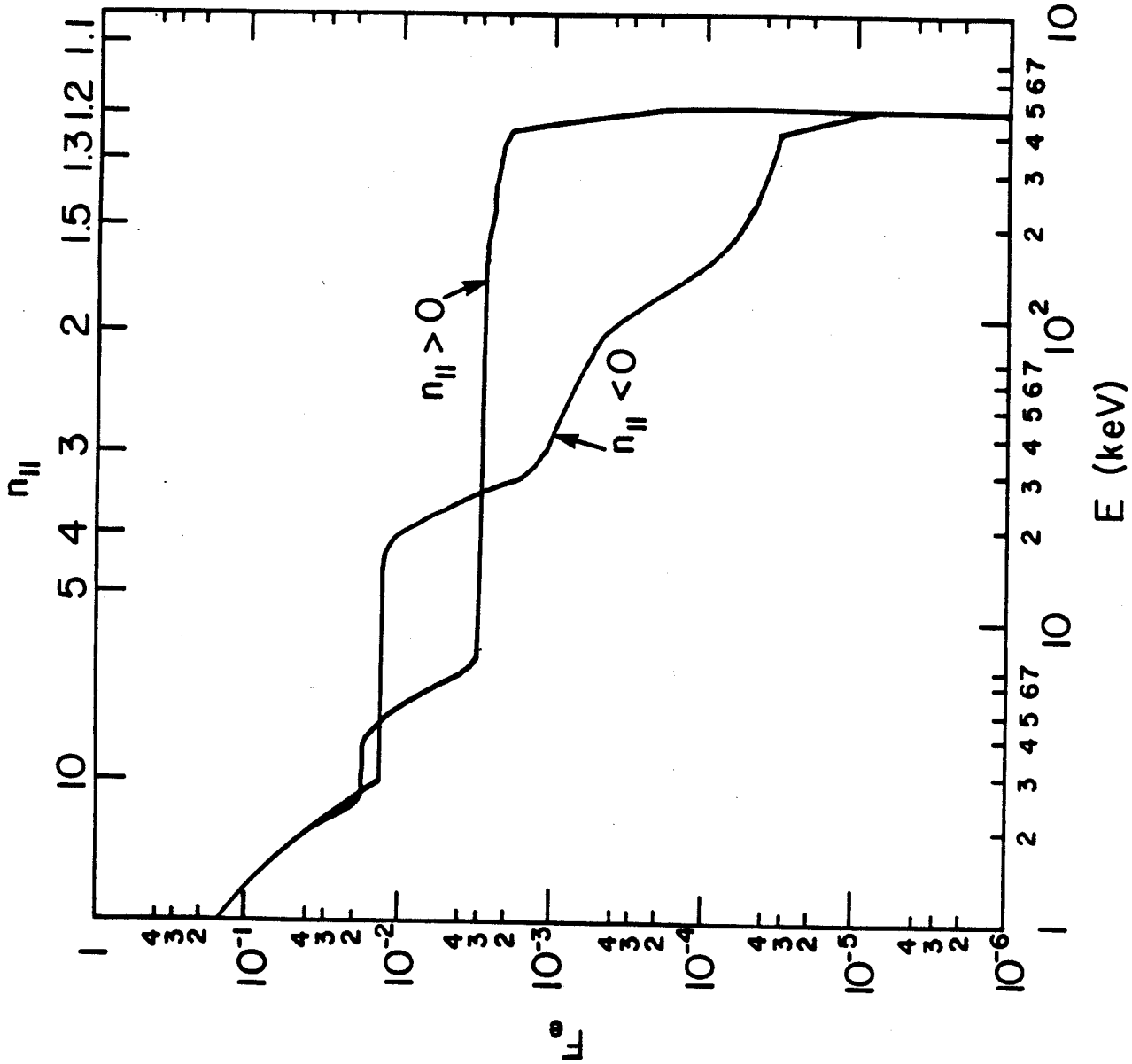
$n_{\parallel}$
10
5
4
3
2
1.5
1.3
1.2
1.1
1
$n_{\parallel} > 0$
$n_{\parallel} < 0$
T_e
10^{-1}
10^{-2}
10^{-3}
10^{-4}
10^{-5}
10^{-6}
E (keV)
10
10^2
10^3

Fig. 10

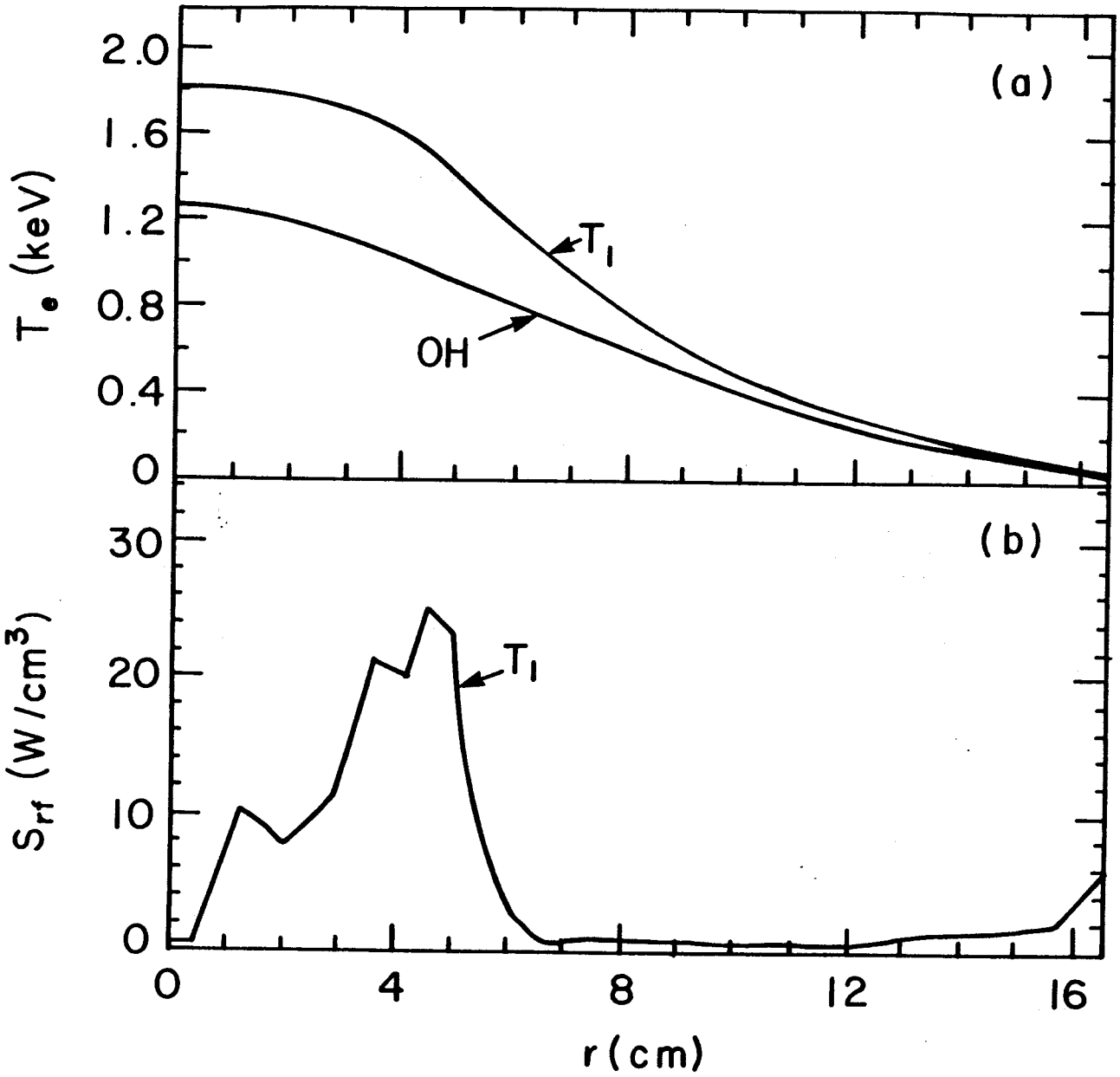

Fig. 11(a,b)

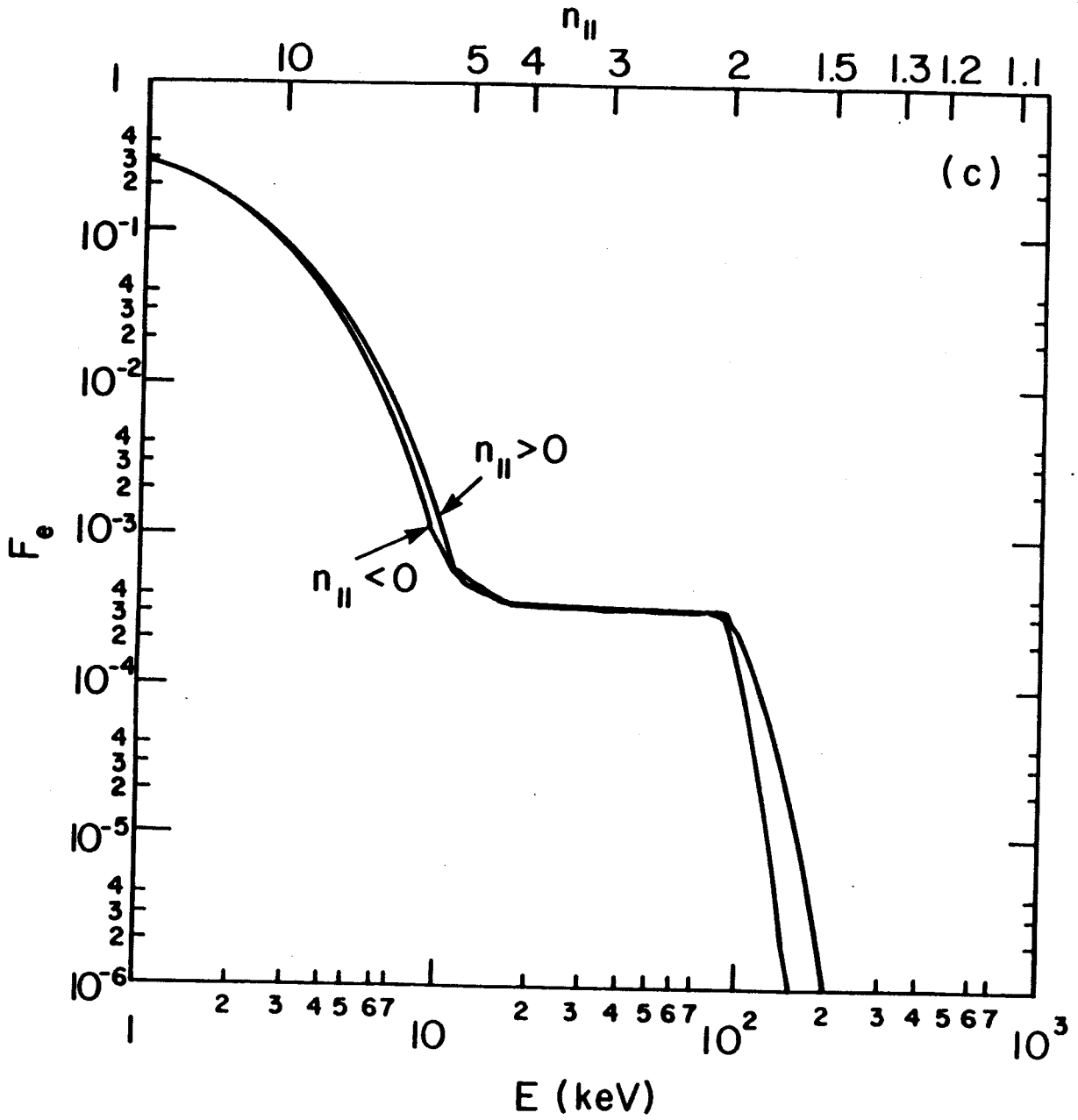
n||
10
5
4
3
2
1.5
1.3
1.2
1.1
1
(c)
10^{-1}
10^{-2}
10^{-3}
10^{-4}
10^{-5}
10^{-6}
F_Φ
$n_{||}>0$
$n_{||}<0$
2 3 4 5 6 7
1
10
10^2
10^3
E (keV)

Fig. 11(c)

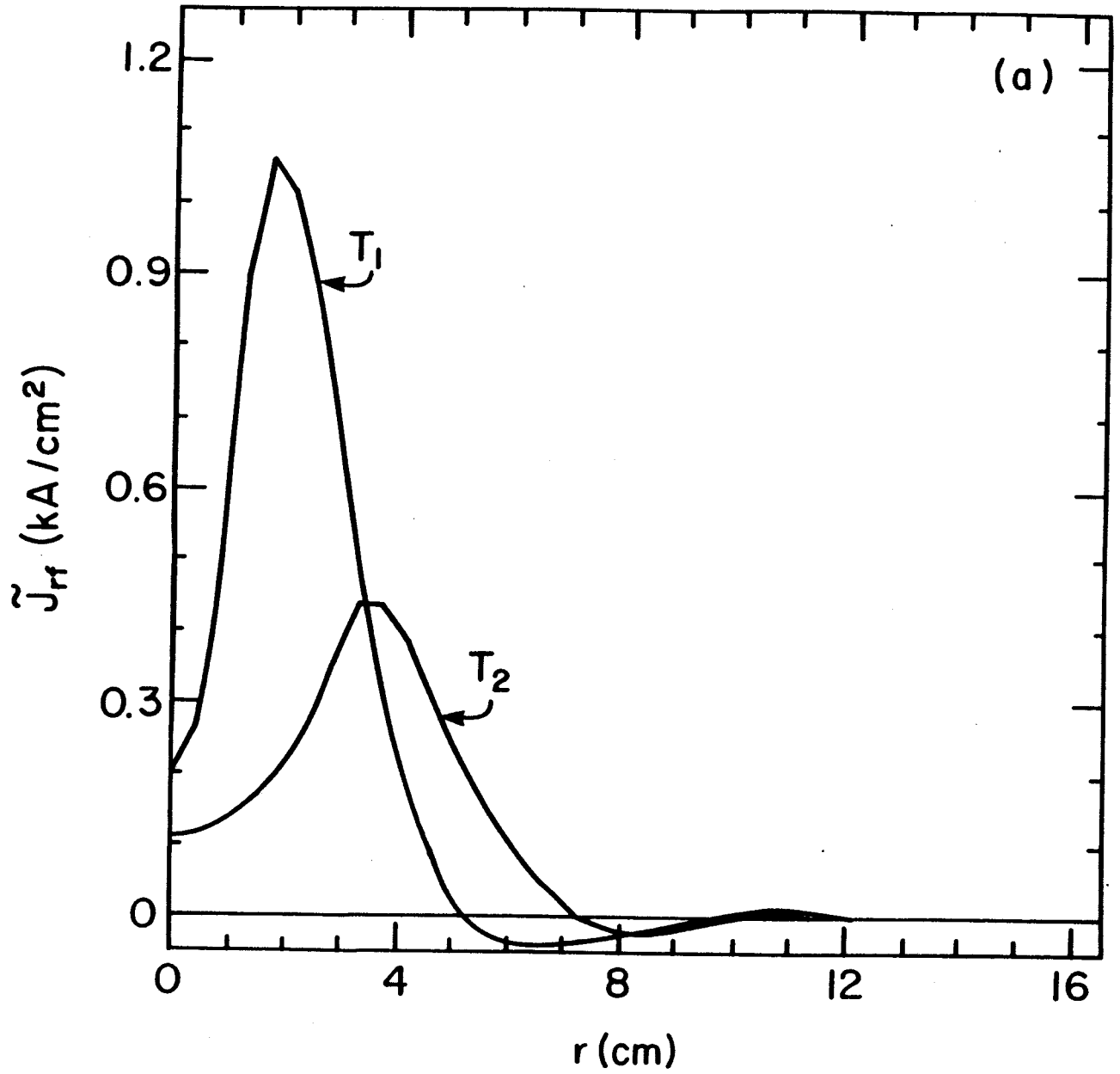

Fig. 12(a)

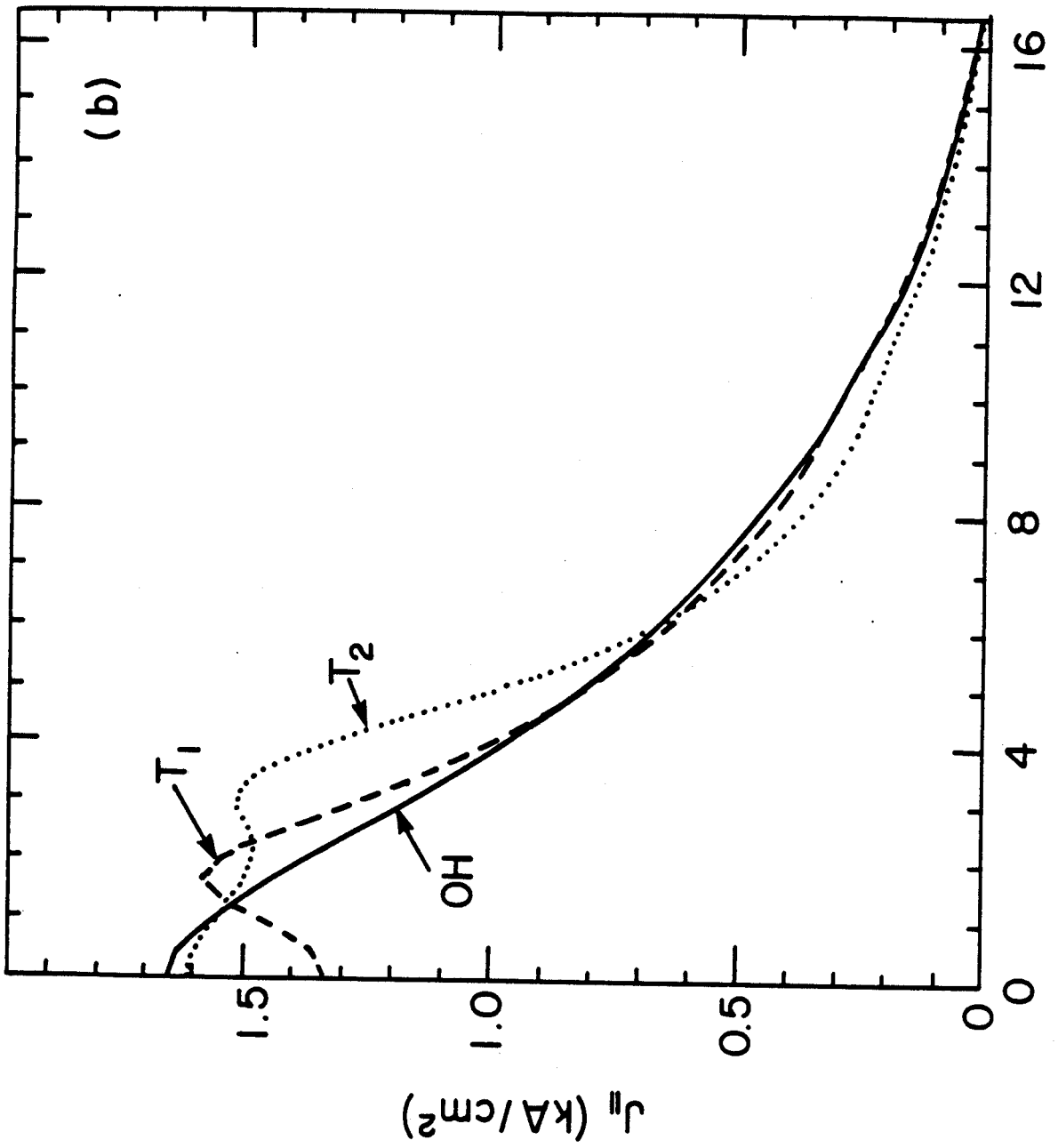

Fig. 12(b)

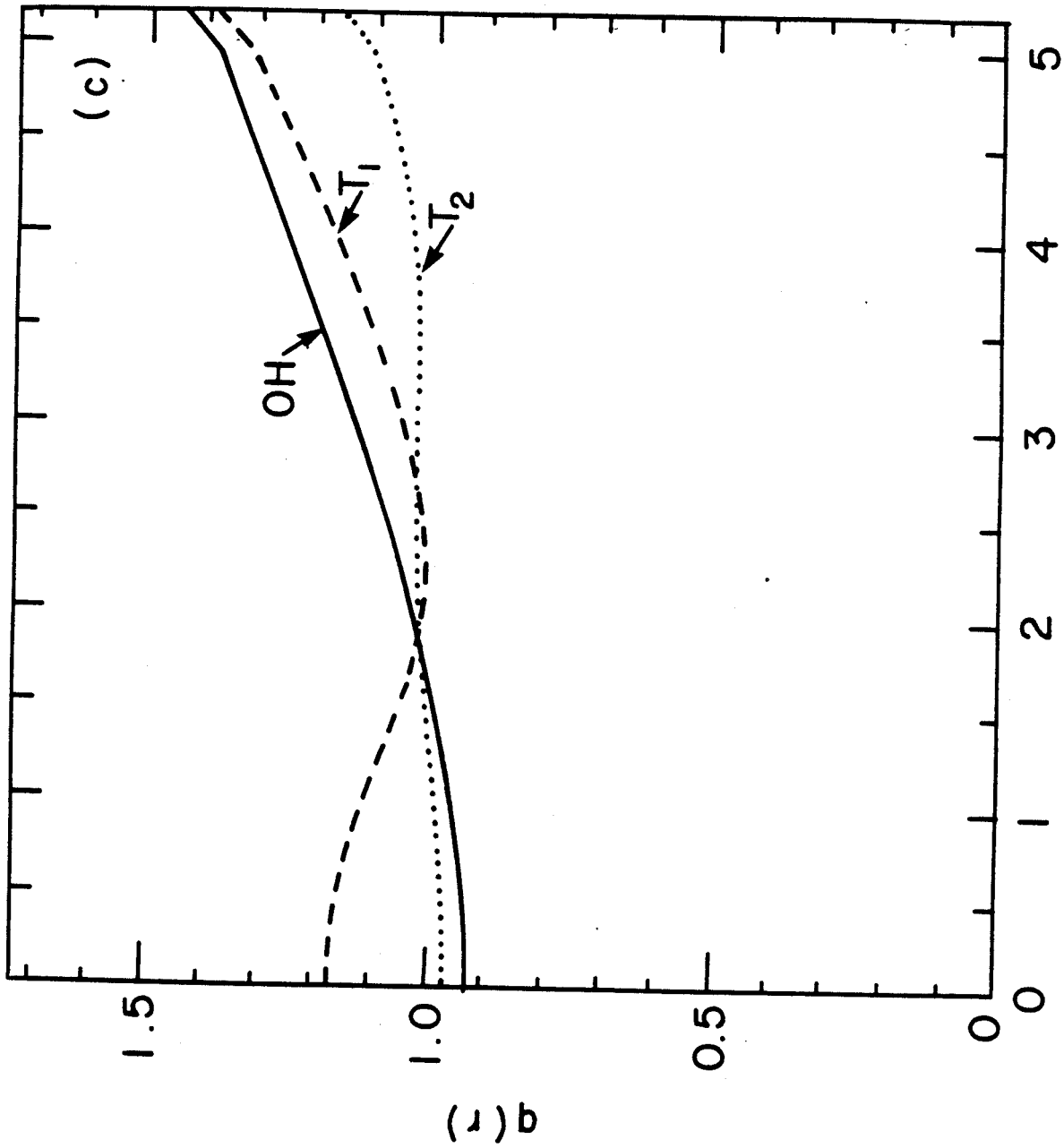

Fig. 12(c)

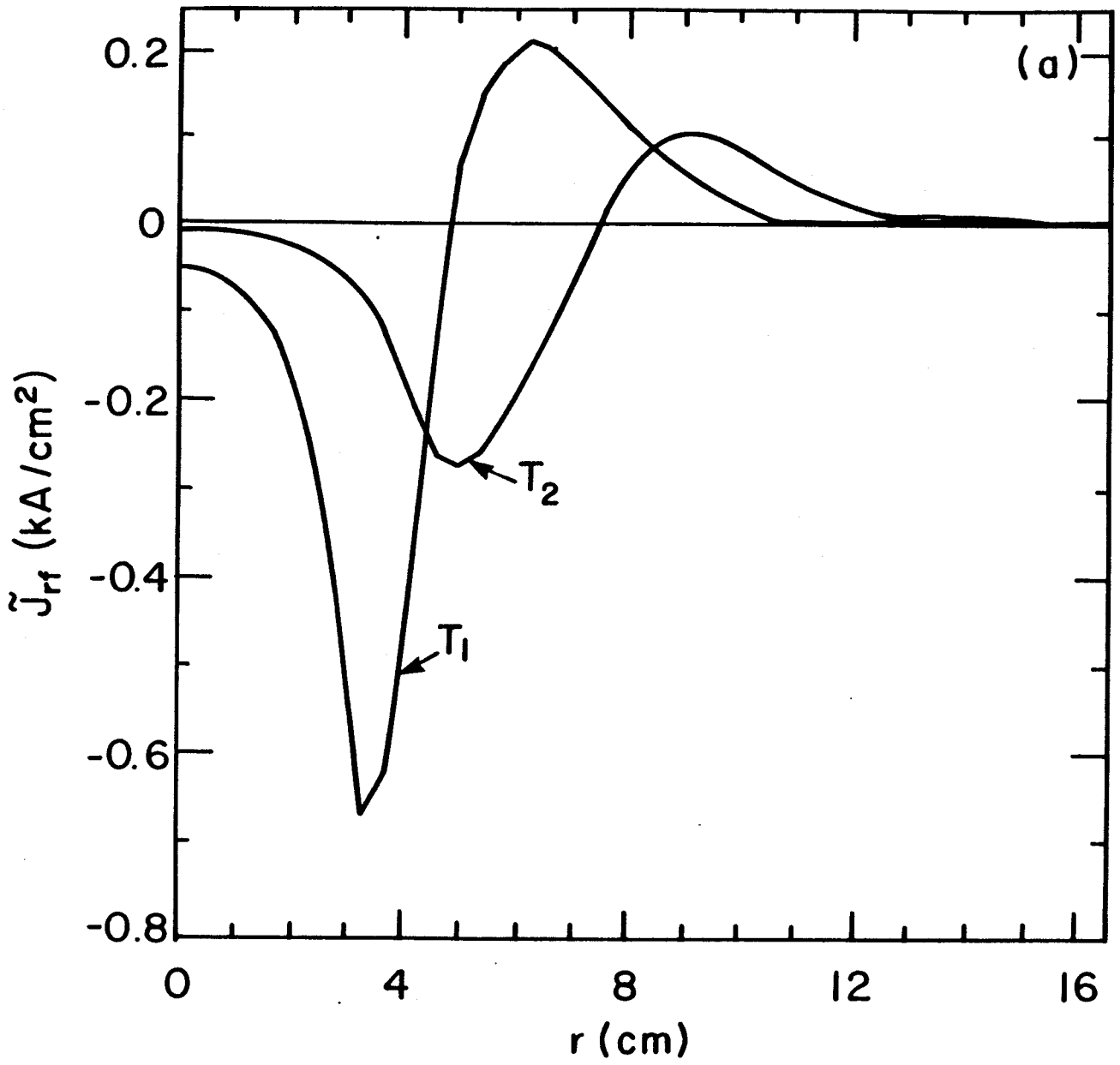

Fig. 13(a)

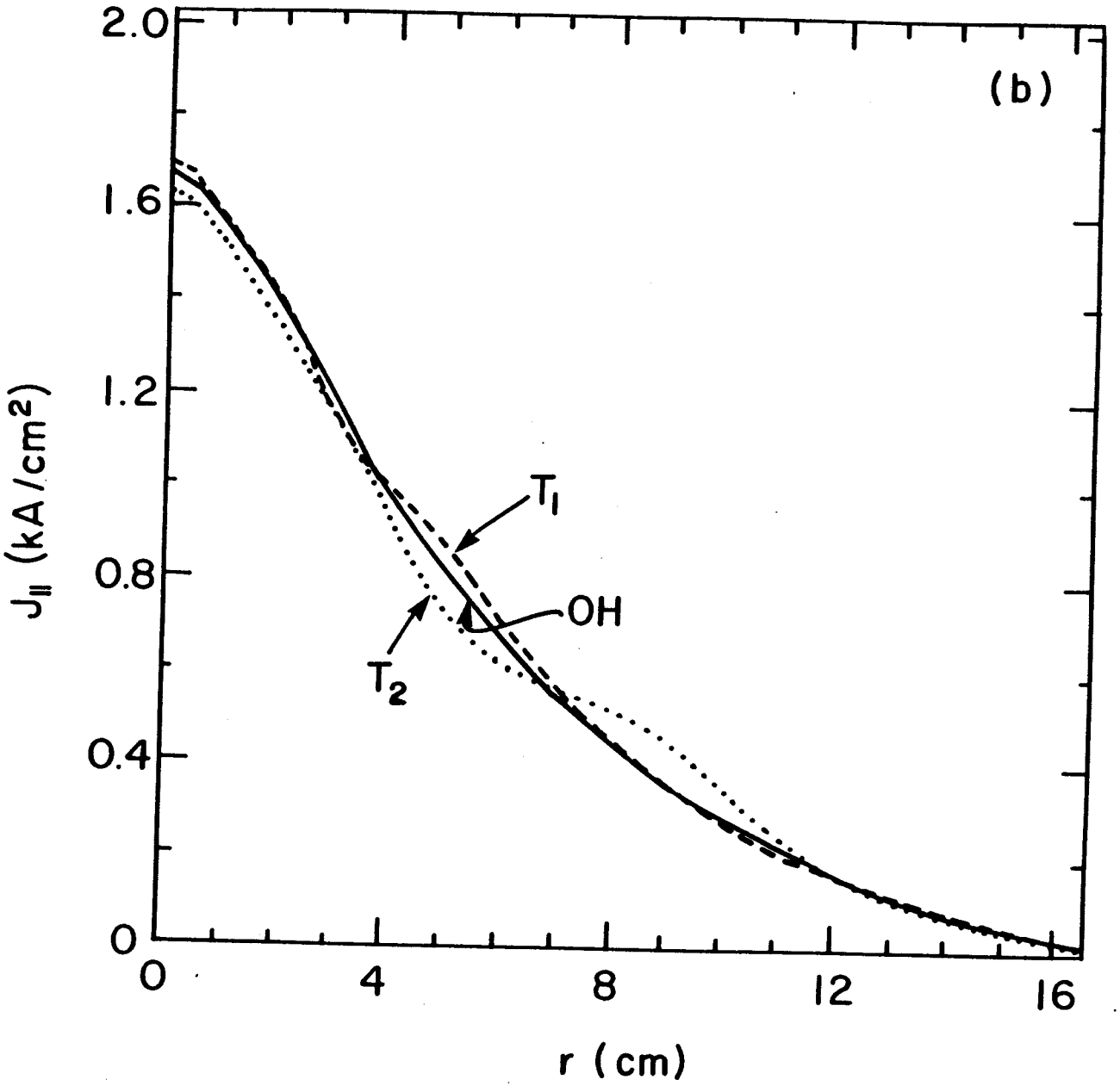

Fig. 13(b)

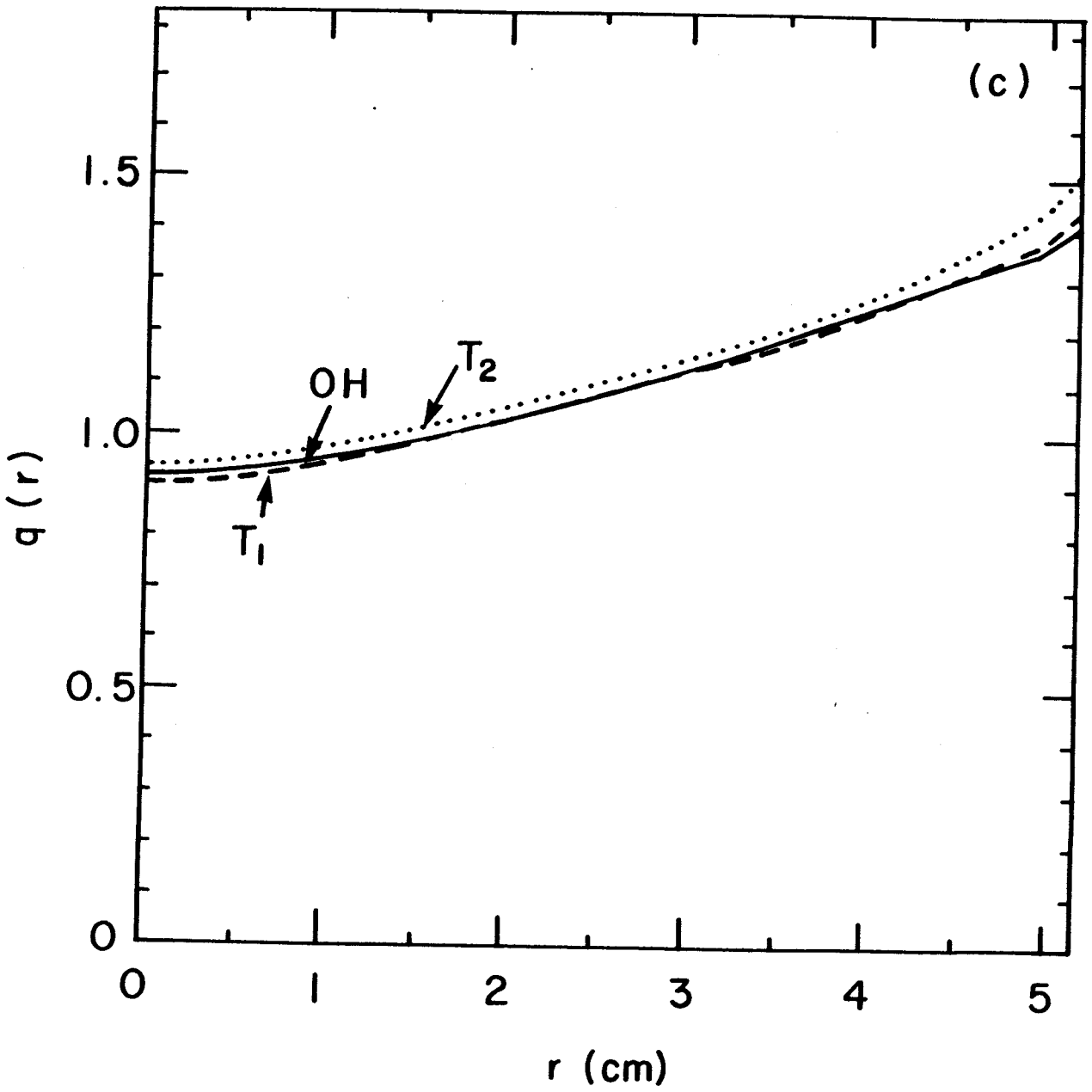

Fig. 13(c)